UC Santa Barbara
UC Santa Barbara Electronic Theses and Dissertations

Title

Insights into the Structure and Dynamics of Human Wnt Signal Transduction

Permalink

https://escholarship.org/uc/item/68r91244

Author

Lach, Ryan

Publication Date

2023

Supplemental Material

https://escholarship.org/uc/item/68r91244#supplemental

Peer reviewed|Thesis/dissertation

University of California

Santa Barbara

Insights into the Structure and Dynamics of Human Wnt Signal Transduction

A dissertation submitted in partial satisfaction
of the requirements for the degree

Doctor of Philosophy
In
Molecular, Cellular & Developmental Biology

by

Ryan Sarsfield Lach

Committee in charge:

Professor Maxwell Z. Wilson, Chair
Professor Kenneth S. Kosik
Professor Denise Montell

December 2023

The Dissertation of Ryan Sarsfield Lach is approved.

_____

Professor Denise Montell

_____

Professor Kenneth S. Kosik

_____

Professor Maxwell Z. Wilson, Committee Chair

September 2023

Insights into the Structure and Dynamics of Human Wnt Signal Transduction

Copyright © 2023

by

Ryan Sarsfield Lach

Acknowledgements

A PhD is in many ways a deeply personal, isolating and somewhat selfish undertaking that absolutely requires long-term patience and support from those around the student. At times, small setbacks and victories alike can feel like the end of the world or winning the Nobel Prize (what I imagine it feels like, at least). This support comes in many flavors: practical, emotional, legal, financial; I have the good fortune to have been on the receiving end of better support than I ever felt I deserved, and I must acknowledge the generous people who have been there to provide it whenever and wherever I have needed it.

First, to my patient and brave advisor, Dr. Max Wilson. You have always seen my potential with more clarity and optimism than I ever could. You inspired me and supported me professionally and academically throughout grad school and have helped me to grow into the scientist I am today. You have a unique vision on what being a scientist is all about and I will never forget your willingness to take me along with you.

To my committee members: Dr. Denise Montell and Dr. Ken Kosik. For your gracious and constructive feedback in yearly meetings and grant proposals and for challenging me to tackle difficult questions during my time in grad school.

To my fellow grad students, friends and surfing buddies (current and former): Erik Hopkins, Taivan Batjargal, Brent Chick, Michael Costello, Markus Merk, Orlando Chirikian M.B.A, Dr. Mohammed Faynus, Dr. Eric Valois, Naomi Baxter, Surenna Pecchia, Zach Aralis, Meg Schimmel, Liz Sharpe, Sam Rosen and Chong Qiu. I would be nothing without your friendship, encouragement and support as peers.

To the brave undergraduates who (as volunteers!) did the real work. Erfan Zeyaei Kajbaf, Hannah Lock, Alex Wang, Courtney Hults and Jose Nunez. Thank you for your patience and trust as I learned to be a graduate mentor and scientific manager.

To my friends outside of graduate school: Baron, Kiah and Jude Santos, Kevin Miller, Ian Pilcher, Jocelyn Toy, Mel and Bryce Randolph, Emily Larson, Nate Nelson Esq., Jack Queen, Sam Huestis, Lucas Bruns, Will Baker, Dr. Hank Zecca, Scot Broadbent, Chandler Hartnett, Gabe De La Rosa, Fletcher Keeley, Adam Levinson, James Conroy, Rachel Fishman, Eve Babcock, Kristi Murray and Lily Biggar. Who have kept in touch from near and far, helped keep my feet on the ground and my head out of the clouds.

To my dog Mac, for always loving, supporting and reminding me that life doesn't have to be that serious.

To my parents, Sally Sarsfield and Jonny Lach. Who raised me with love and compassion and never tried to talk me into being someone other than myself.

To my brother, Griffin Lach, for reminding me that I'll always be (at most) the 2nd smartest person in the room when he's around, regardless of whatever fancy degree I have. Go Jets.

Finally, to my fiancé Erin Platt, the kindest and strongest person I know and who has given endless love and perspective as I have moved throughout this journey. I love you and will never be able to repay you for the role you have played in getting me here. Thank you all.

Curriculum Vitae

Ryan Sarsfield Lach

Education

2023 Ph.D in Molecular Biology, University of California, Santa Barbara
2016 B.A. in Neuroscience, Colorado College

Honors and Awards

2020 – 2023 Eunice Kennedy Shriver National Institute for Childhood Health and Development, National Institutes of Health, F31 National Research Service Award

2021 Fiona and Michael Goodchild Award, University of California, Santa Barbara

2019 Storke Graduate Fellowship Award, University of California, Santa Barbara

Publications

- <u>Lach RS</u>, Qiu C, Kajbaf EZ, Baxter N, Han D, Wang A, Lock H, Chirikian O, Pruitt B, Wilson MZ. Nucleation of the destruction complex on the centrosome accelerates degradation of β-catenin and regulates Wnt signal transmission. Proc Natl Acad Sci U S A. 2022 Sep 6;119(36):e2204688119. doi: 10.1073/pnas.2204688119. Epub 2022 Aug 29. PMID: 36037369; PMCID: PMC9457612.

- Aralis Z, Rauch JN, Audouard M, Valois E, <u>Lach RS</u>, Solley S, Baxter NJ, Kosik KS, Wilson MZ, Acosta-Alvear D, Arias C. CREST, a Cas13-Based, Rugged, Equitable, Scalable Testing (CREST) for SARS-CoV-2 Detection in Patient Samples. Curr Protoc. 2022 Feb;2(2):e385. doi: 10.1002/cpz1.385. PMID: 35195954.

- Rauch JN, Valois E, Solley SC, Braig F, <u>Lach RS</u>, Audouard M, Ponce-Rojas JC, Costello MS, Baxter NJ, Kosik KS, Arias C, Acosta-Alvear D, Wilson MZ. A Scalable, Easy-to-Deploy Protocol for Cas13-Based Detection of SARS-CoV-2 Genetic Material. J Clin Microbiol. 2021 Mar 19;59(4):e02402-20. doi: 10.1128/JCM.02402-20. PMID: 33478979; PMCID: PMC8092748.

- Rauch JN, Valois E, Ponce-Rojas JC, et al. Comparison of Severe Acute Respiratory Syndrome Coronavirus 2 Screening Using Reverse Transcriptase–Quantitative Polymerase Chain Reaction or CRISPR-Based Assays in Asymptomatic College Students. *JAMA Netw Open.* 2021;4(2):e2037129. doi:10.1001/jamanetworkopen.2020.37129

Abstract

Insights into the Structure and Dynamics of Human Wnt Signal Transduction

Ryan Sarsfield Lach

The Wnt pathway is essential for the healthy construction and maintenance of the metazoan anatomy and initiates carcinogenesis when dysregulated. Though a rich body of work on tissue- and organ-level roles of key pathway components exists, relatively little is known about the intracellular mechanisms that transduce Wnt signals into changes in cell behavior and identity. This dissertation project was conceived with two guiding goals: 1) characterize the native structure and function of the canonical Wnt pathway in human cells, and 2) determine how Wnt signaling dynamics are relayed through the pathway into cell fate decisions.

Using CRISPR-Cas9 gene editing, super-resolution microscopy, optogenetics and computational modeling, we find that the central regulator of Wnt signal transduction, the β-catenin (β-cat) Destruction Complex (DC), exists in liquid-like condensates nucleated by the centrosome. Our results suggest that centrosomal nucleation drives β-cat degradation by lowering the concentration threshold required for condensate formation, locally enriching DC components compared to the cytoplasmic dilute phase. This work is covered in depth in Chapter 2.

In Chapter 3 I incorporate live reporters of cell cycle progression, high content single-cell tracking and dynamical inputs to construct a systems-level understanding of intracellular Wnt signal transduction and differentiation. This approach revealed that unsynchronized cell populations respond heterogeneously to Wnt stimulation,

and that transcriptional response trajectory can be predicted by the cell cycle phase in which stimulus is withdrawn. We find evidence that Wnt "off-time sensing" tunes the pathway to specific input frequencies, a capability that may protect against carcinogenic Wnt secretion states.

This work provides novel insights into the architecture, functions and vulnerabilities of human Wnt signaling. Despite its clear connection to these processes, there are no FDA-approved therapeutics that leverage the Wnt pathway to regenerate damaged tissues or treat cancer. By adding to our understanding of Wnt signal transduction, I hope to assist in the development of working knowledge we may leverage for treating Wnt-driven pathologies.

Contents

Chapter 1

Introduction

Towards a Systems-level Understanding of Morphogenesis

Multicellular organisms are constructed and maintained via a series of pre-programmed and adaptive morphogenic decisions made by individual cells to survive, proliferate, migrate and differentiate[1]. Tissues emerge from ensembles of individual cells utilizing morphogenic decisions to cooperatively direct and monitor the function of stable, higher-order structures. Tissues both build the body during development and provide it with specialized capabilities that promote environmental fitness in maturity. Morphogenesis is essential for the rich diversity of forms and functions we observe in eukaryotes[2]; an improved understanding of the underlying mechanisms of morphogenesis will both strengthen our knowledge of the biological world around us and promote the development of life-saving therapeutics.

Morphogenesis is complex: tissue-level decisions are the sum of millions of individual cellular decisions, which are themselves the sum of the activity of tens of millions of proteins in a single cell[3]. Even if a comprehensive, granular model of this network existed, present computational limitations would prevent its practical use in predicting, for example, the full effect of a small mutation in a gene implicated in cancer. In the face of this daunting complexity, biologists have traditionally focused on either the high-level effects of gain/loss of function interventions on proteins of interest, or on simple, local biological systems suitable for mathematical modeling. Recent advances in microscopy and synthetic biology have enabled the utilization of

precise biological inputs and rich data outputs for modeling more complex and broadly applicable systems such as morphogenesis[4]. Predictive models of more complex intracellular and tissue-level processes that control morphogenesis will provide invaluable insights into the design principles, functional advantages and weaknesses of these systems. Knowledge of these mechanisms will facilitate targeted repair of disease-causing states and even *de novo* regeneration of damaged biological tissue.

This dissertation—via precision gene editing, optogenetics, super-resolution microscopy and computational modeling—seeks to elucidate the mechanisms by which a conserved eukaryotic system, the canonical Wnt pathway, transduces essential morphogenic information both at the levels of single cells and tissues.

The Canonical Wnt Pathway in Development, Homeostasis and Disease

Signaling networks transduce external information into cellular responses that construct and maintain the human body. Biochemical signals encoding representations of the extracellular environment inform the cell of its position, identity, and purpose in developing and adult tissues. Faithful transmission of these signals directs proper morphogenesis, repair and homeostasis while faulty signal transmission leads to cellular misinformation, improper development, inadequate regeneration and cancer. A deep understanding of the components and design principles of signaling networks thus reveals modes of failure and leads to novel therapeutic solutions that address these problems.

The canonical Wnt pathway is among the most highly conserved[5] and consequential of these signaling networks. This pathway transmits a broad set of cellular instructions using Wnt ligands expressed in spatiotemporal morphogenic patterns throughout development. Notably, spatial patterns of Wnt specify cell fate during healthy embryogenesis and adult tissue maintenance, while Wnt pathway dysfunction leads to pathologies ranging from neurodegeneration[6] to cancer[7]. Despite the pathway's importance to health, Wnt signal transmission remains poorly understood.

A major reason for this knowledge gap is the complex and atypical organization of intracellular Wnt signal transduction. The Wnt pathway is not a typical signaling cascade that relays extracellular information to the nucleus via sequential phosphorylation of tiered kinases. Rather, it appears to integrate multiple enzyme activities through a meso-scale organelle, called the Destruction Complex (DC), which constitutively degrades a key transcription factor, β-catenin (β-cat)[8] (***Fig. 1.1***)*.* When Wnt ligand is absent, a low cytoplasmic concentration of β-cat is maintained, preventing its activation of Wnt-target genes. In response to Wnt, the DC's ability to process β-cat is inhibited through an unknown mechanism, resulting in nuclear translocation of β-cat and activation of the Wnt ON transcriptional program.

Previous work trying to understand the role of the DC in Wnt signaling has focused on measurements performed in fixed specimens with over-expressed components. These experiments fail to capture the dynamic transitions between signaling states at endogenous expression levels. It has recently been suggested

3
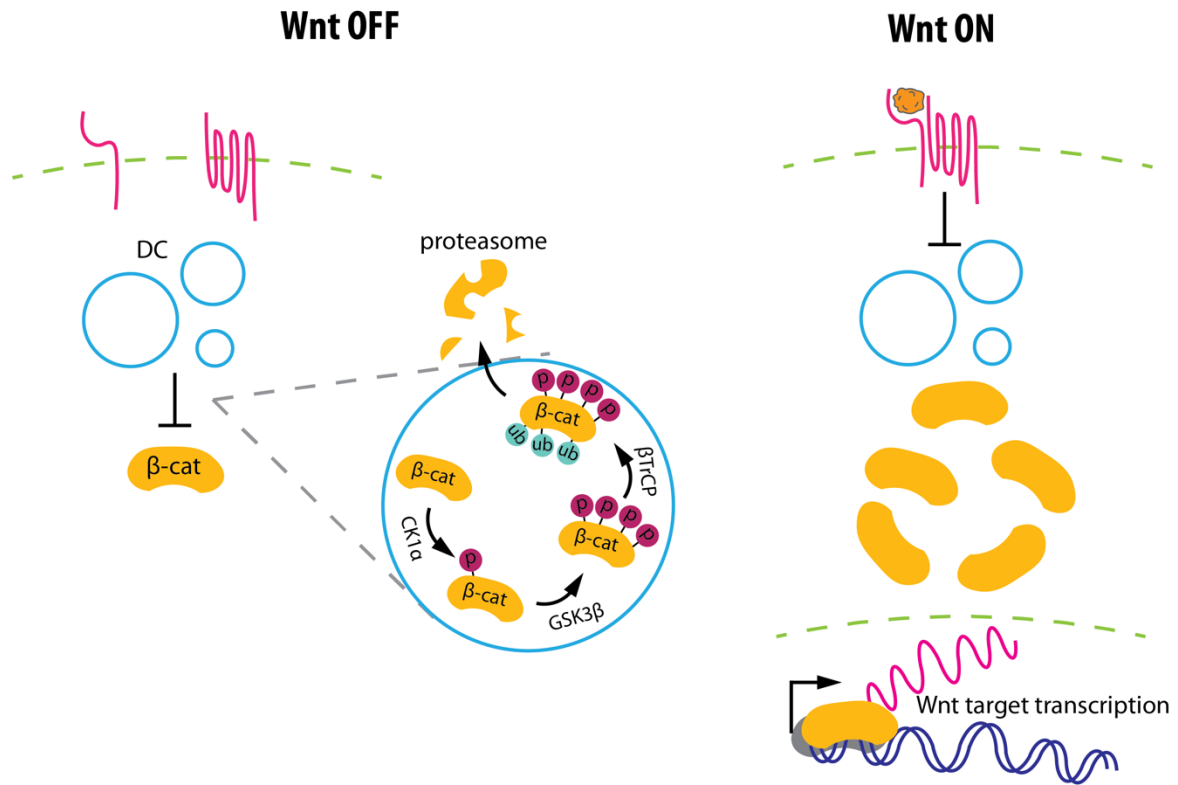
Figure 1.1: Schematic of the canonical Wnt pathway. *Left:* When Wnt ligands are absent the β-catenin (β-cat) destruction complex (DC) catalyzes sequential phosphorylation of β-cat by CK1α and GSK3β then polyubiquitination by βTrCP. Concentration of reactants and catalysts in liquid-liquid phase separated (LLPS) droplets is thought to accelerate β-cat flux through this cycle. *Right:* In the presence of Wnt ligands, the DC is inhibited and β-cat accumulates in the cytoplasm and nucleus. Increased nuclear concentration of β-cat induces transcriptional activation of Wnt target genes.

that DC function is related to its ability to undergo liquid-liquid phase separation (LLPS) to form droplets thought to solvate monomeric β-cat and catalyze its degradation[9]. Given the sensitivity of protein scaffold concentration in determining phase state (dense or diffuse)[10], it is essential to carefully control (and not simply over-express) the DC scaffolds to study their role in using phase to transmit Wnt signals.

Liquid-liquid Phase Separation in Wnt Signal Transduction

LLPS has emerged as an important biophysical process by which cells monitor, compartmentalize and regulate local concentrations of intrinsically-disordered proteins (IDPs). Similar to the two-phase system observed when oil and vinegar are mixed in salad dressing, IDPs tend to de-mix from folded proteins solvated by the cytosol, forming large, dynamic droplets[11]. Cells control the concentration and valency of IDPs to form phase-separated membraneless organelles—such as stress granules[12]—when they are needed, and dissolve them when they are not[13].

LLPS offers an intriguing mechanism by which large, switch-like spatiotemporal rearrangements of proteins can be controlled by the cell, but many key questions surrounding its function in signaling pathways remain: 1) What are the contents of LLPS droplets? IDP 'scaffolds' are typically and large and multivalent, containing multiple folded and unfolded binding sites that recruit a diverse network of other scaffolds and singly-valent 'clients' to the dense phase[14]. These networks are found to contain thousands of unique proteins[15], making an exhaustive catalog of interaction partners for a given LLPS condensate difficult to construct. 2) What are the mechanisms underlying control of LLPS and how are these used in their native contexts? Most work in the field of biological LLPS has been characterizing phase boundaries of single IDPs _in vitro_—determining whether a given protein's propensity to de-mix is affected by changing electrostatic interactions with the solvent, non-polar interactions with itself or truncation of important domains. These characteristics are fundamental but add little to our understanding of network dynamics in the cell; technologies for probing the role of LLPS _in situ_ are needed to better address this

open question. 3) How is LLPS used in signal transduction? It is clear that phase

separation changes how scaffolds and clients interact with their binding partners, but

what functionality this imparts on associated signaling pathways is still largely

unknown. This dissertation aims to further our understanding of LLPS by answering

these questions using the Wnt pathway as a model system.

Much of our contemporary understanding of the importance of LLPS in Wnt

signaling architecture comes from the discovery that approximately 70% of

colorectal cancers originate from mutations in the IDP scaffolds Adenomatous

polyposis coli (APC) and Axin[16]. Axin and APC are essential for efficient β-catenin

degradation, recruiting the kinases CK1α and GSK3β, and the ubiquitin ligase

βTrCP to nascent β-catenin molecules for post-translational modification and

subsequent degradation. Both Axin and APC contain long intrinsically-disordered

regions (IDRs) and undergo LLPS in healthy cells[9,17], forming dense, viscous

droplets thought to concentrate β-catenin with the aforementioned DC enzymes[8].

Mutations that obstruct LLPS of either DC scaffold (without disturbing binding sites

for enzymes or β-catenin) result in high levels of β-catenin and pathway activation in

the absence of ligand and a persistent Wnt-ON oncogenic phenotype. Intriguingly,

experiments in colorectal cancer cell lines in which APC truncations hinder DC LLPS

showed that Axin overexpression was able to compensate for this phenotype,

restoring droplet formation and lowering cytoplasmic β-catenin levels[18]. These

findings have recently given rise to the idea that the high level of β-catenin that

accompanies oncogenesis is due to a loss of the DC's ability to LLPS and efficiently

drive its degradation. Similarly, we reasoned that changes in DC LLPS may also underly β-cat disinhibition in healthy cells in the presence of Wnt ligand.

Chapter 2

Nucleation of the destruction complex on the centrosome accelerates degradation of β-catenin and regulates Wnt signal transmission

Abstract

Wnt signal transduction is controlled by the Destruction Complex (DC), a condensate comprised of scaffold proteins and kinases that regulate β-catenin stability. Overexpressed DC scaffolds undergo liquid-liquid phase separation (LLPS), but DC mesoscale organization at endogenous expression levels and its role in β-catenin processing were previously unknown. Here, we find that DC LLPS is nucleated by the centrosome. Through a combination of CRISPR-engineered custom fluorescent tags, finite element simulations, and optogenetic tools that allow for manipulation of DC concentration and multivalency, we find that centrosomal nucleation drives processing of β-catenin by co-localizing DC components to a single reaction crucible. Enriching GSK3β partitioning on the centrosome controls β-catenin processing and prevents Wnt-driven embryonic stem cell differentiation to mesoderm. Our findings demonstrate the role of nucleators in controlling biomolecular condensates and suggest tight integration between Wnt signal transduction and the cell cycle.

Introduction

The canonical Wnt signaling pathway is a conserved[5], morphogenic pathway that is essential for embryonic development, maintains adult tissue homeostasis, and, when dysregulated, induces malignancies[7,19,20]. Wnt signals converge onto a protein assembly called the destruction complex (DC), which tunes the stability of β-catenin (β-cat), the pathway's central transcriptional effector, by regulating its interactions with the kinases, CK1α and GSK3β, and the ubiquitinase, β-TRCP, which directs β-cat to the ubiquitin-mediated proteolysis machinery. Despite the DC's role in regulating β-cat stability, the structural principles that underly its functioning in development and disease are still poorly understood.

Extracellular Wnt ligands inhibit DC function through a mechanism that is still unclear, but likely involves selective recruitment of DC components to the signalosome, a biomolecular condensate on the plasma membrane that includes Wnt/Frizzled/LRP5/6 clusters[21]. Optogenetic clustering of LRP5/6 is sufficient to stabilize β-cat[22], suggesting the formation of mesoscale protein clusters at the Wnt receptor level is necessary and sufficient for activating the pathway. Less is known about the DC's native structure and how it maintains low β-cat levels in the Wnt OFF state. Recently, the DC scaffolds Axin and Adenomatous Polyposis Coli (APC), and the signalosome "adapter" protein Disheveled have been shown to undergo liquid-liquid phase separation (LLPS) *in vitro*[23] and, when exogenously over-expressed, *in vivo*[17,24,25]. Cancer-causing mutations that eliminate Axin or APC LLPS are correlated with aberrant accumulation of β-cat[8,26] and can be rescued by orthogonal

protein-multimerizing domains[27]. These studies raise the question: what is the role of mesoscale assembly of the cytoplasmic DC components in regulating β-cat stability?

The "molecular crucible" model posits that DC LLPS promotes β-cat degradation in Wnt OFF conditions[23] via concentration of DC clients (CK1α, GSK3β, and β-cat) in DC scaffold (Axin and APC) condensates to increase the rate of β-cat processing. LLPS-mediated DC concentration is distinct from theories suggesting that the DC acts as an ordered, assembly-line-like scaffold akin to Ste5 in the yeast MAPK pathway[28]. Indeed, deletions in Axin regions that promote LLPS[21] increase β-cat stability[23]. In this paradigm, conditions that alter the phase behavior of scaffolds and partitioning of clients are predicted to regulate the stability of β-cat and Wnt signal transmission.

A biophysical mechanism for regulating condensates is control over their nucleation. This principle was recently explored with a synthetic optogenetic system[29], but the role of nucleation in natural biological processes remains unknown. Phase separating systems exhibit switch-like responses to changes in concentration[30,31] and often exist near these transitions *in vivo*[32,33]. Dissecting the mechanisms controlling LLPS requires control over protein concentration and affinity, and overexpression of DC components may not recapitulate endogenous mesoscale structure. Here, we utilize CRISPR gene editing, custom inducible expression vectors, and optogenetic tools to observe and probe the native, mesoscale organization of the DC in the Wnt OFF and Wnt ON states.

Building on results demonstrating that β-cat[34,35], Axin1[36], APC[37] and βTrCP/*Slimb*[38] localize to the centrosome, we show that all DC components are

nucleated by the centrosome into liquid-like biomolecular condensates. In support of the molecular crucible theory, we find that nucleation drives efficient degradation of β-cat. We utilize a Cahn-Hilliard-based simulation of DC droplet formation and enzyme kinetics to predict how nucleation and affinity of DC components promotes efficient β-cat processing. Finally, using our model as a guide, we engineered a light-inducible GSK3β (Opto-GSK3) to control partitioning at the centrosome, β-cat degradation, and stem cell differentiation into mesoderm. These findings show that DC droplet formation is nucleated by the centrosome and suggest that DC scaffolds function to concentrate clients in liquid droplets *in vivo* to accelerate the degradation of β-cat.

Results

<u>*β-catenin condensation is predictive of Wnt pathway activity state*</u>

To understand the role of mesoscale organization in DC function, we first sought to characterize the DC's main substrate, β-cat in live cells. We used CRISPR to knock in a custom fluorescent tag, tdmRuby3, to the *CTNNB1* gene of 293T cells (**Fig. 2.1A**). Live-cell confocal imaging revealed expected cytoplasmic accumulation in response to Wnt-3a ligand and the GSK3β inhibitor CHIR (**Supp. Fig. 2.1A-B, Supp. Vid. 1**) and localization of β-cat at the cell membrane, consistent with previous work in fixed specimens[39]. In addition, we observed that most cells contained 1-2 bright, spherical, perinuclear β-cat puncta (**Fig. 2.1B** *top left*). Timelapses showed fission and fusion of puncta on the timescale of minut es (**Fig.**

2.1M), suggesting that these structures are liquid-like biomolecular condensates.

Given the prevalence of biomolecular
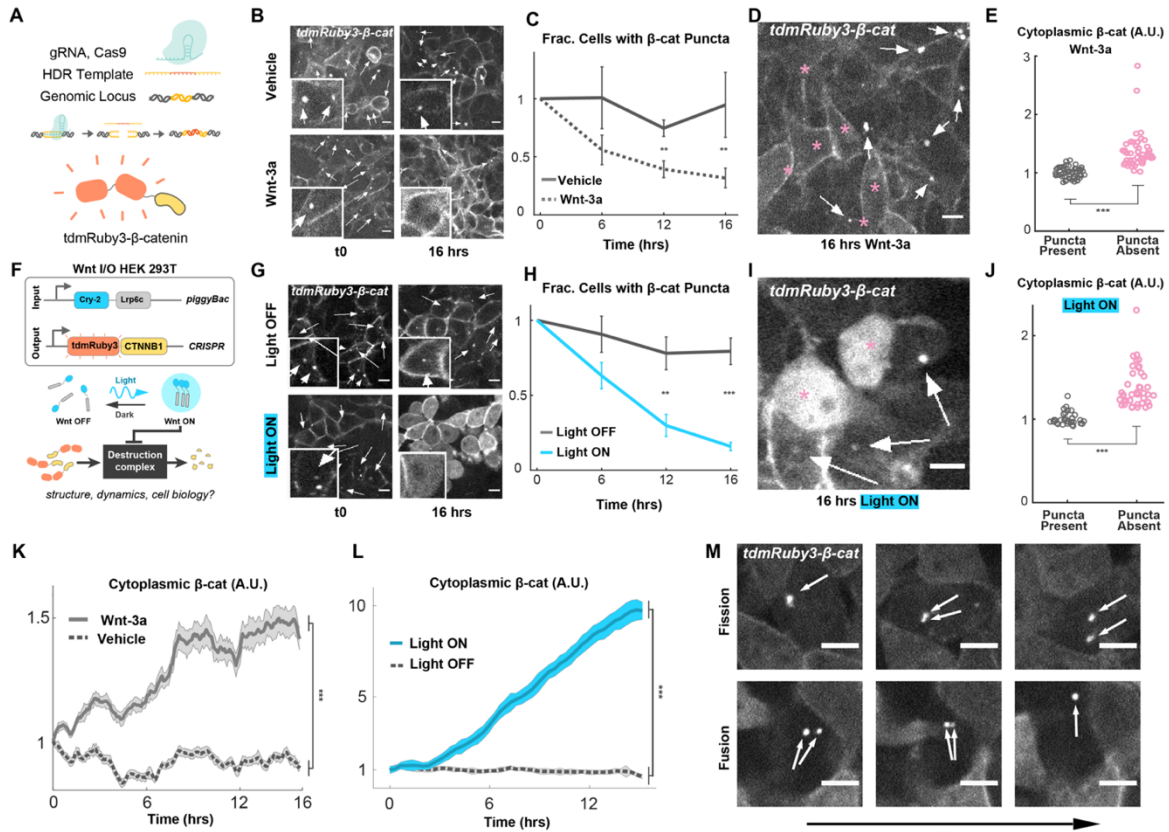
Figure 2.1: Endogenously expressed β-catenin puncta are inversely correlated with lrp6-mediated Wnt pathway activation and β-catenin accumulation. A. Schematic of tdmRuby3 CRISPR tag strategy. **B.** Representative tdmRuby3-β-catenin images of cells treated with Wnt-3a or media vehicle. Arrows indicate β-catenin puncta. Scale = 10µm. **C.** Fraction of t0 population with visible β-catenin puncta, presented as mean +/- s.e.m. (N=12 imaging fields per condition). **D.** Representative cells from Wnt-3a condition. Arrows indicate puncta, asterisks indicate cells lacking puncta. **E.** Comparison of mean cytoplasmic β-catenin fluorescence between Wnt-3a cells with and without visible β-catenin puncta. **F.** Schematic of Wnt I/O cells containing lentivirally-expressed Cry2-LRP6c and CRISPR-tagged tdmRuby3-β-catenin. Stimulation of Cry-2-Lrp6c with blue light results in reversible clustering of lrp6c and downstream pathway activation. **G.** Representative tdmRuby3-β-catenin images of cells stimulated with blue light or left in the dark throughout imaging timecourse. **H.** Fraction of t0 population with visible β-catenin puncta, presented as mean +/- s.e.m. (N=12 imaging fields per condition). **I.** Representative cells from Wnt-3a condition. Arrows indicate puncta, asterisks indicate cells lacking puncta. **J.** Comparison of mean cytoplasmic β-catenin fluorescence between Light ON cells with and without visible β-catenin puncta. **K-L.** Measurements of CRISPR cytoplasmic tdmRuby3-β-catenin in live 293Ts, data presented as mean fluorescent intensity fraction of t0 +/- s.e.m. (N = 30 cells per condition). **M.** Timecourse montage of single CHIR+ cells containing β-catenin puncta undergoing dynamic fission and fusion. Images from consecutive frames of timecourse, 5 minute interval between each.

condensates in organizing important biological processes, we hypothesized that

these perinuclear puncta might organize β-cat destruction.

To determine if Wnt pathway activation altered the perinuclear puncta, we performed volumetric confocal timelapse microscopy on our *tdmRuby3-β-cat* cells and quantified the fraction of cells with puncta as a function of Wnt-3a ligand treatment and time. At the population level, the fraction of cells with puncta significantly decreased in response to Wnt-3a (**Fig. 2.1C**). We found this same relationship existed between single cells in an isogenic population: non-responding cells maintaining their puncta and responding cells dissolving them (**Fig. 2.1D-E**). Thus, the disappearance of perinuclear β-cat puncta is correlated with β-cat accumulation, and the existence of these puncta is correlated to the resistance of ligand-induced accumulation.

To establish if directly activating the Wnt receptor controls the existence of the puncta, we transduced *tdmRuby3-β-cat* cells with an optogenetic version of the Wnt co-receptor, LRP6c (Opto-LRP6)[22]. Opto-LRP6 induced greater accumulation of β-cat than either Wnt or CHIR (**Fig. 2.1K-L**). We thus reasoned that this all-optical Wnt input control and output visualization cell line would maximize our ability to observe rearrangements in pathway components due to a higher dynamic range of activation (**Fig. 2.1F**). We found that activating Opto-LRP6 resulted in a greater reduction in the fraction of cells containing β-cat puncta than treating cells with ligand (**Fig. 2.1G-H, Supp. Vid. 2-3**). β-cat puncta became more difficult to distinguish at higher cytoplasmic concentrations produced by activated Opto-LRP6, but dissolution nearly always preceded appreciable dilute-phase β-cat accumulation, indicating that they were not simply obscured by higher background levels. Further, of light-stimulated cells, those that were resistant to optogenetic activation

maintained their β-cat puncta (**Fig. 2.1 I-J**). We also observed this same resistance to β-cat accumulation in response to CHIR (**Supp Fig. 2.1B**). Together, these results indicate that activation of the Wnt pathway causes perinuclear puncta to dissolve, and the presence of these puncta is inversely related to Wnt pathway activation at the population and single-cell levels.

The destruction complex forms a biomolecular condensate co-localized to the centrosome

We next sought to determine (i) what, if any, cellular structure was organizing these puncta, (ii) if all DC components were co-localized with puncta, and (iii) whether these were solid or liquid-like condensates. Because of the sensitivity of LLPS systems to protein concentration[40], we decided on a strategy that allowed for visualization of DC components at low or endogenous concentrations, while retaining the ability to assess protein dynamics through live-cell microscopy and Fluorescence Recovery After Photobleaching (FRAP). Indeed, DC scaffolds APC and Axin1 form multiple liquid droplets when overexpressed[26,41]. Thus, we used
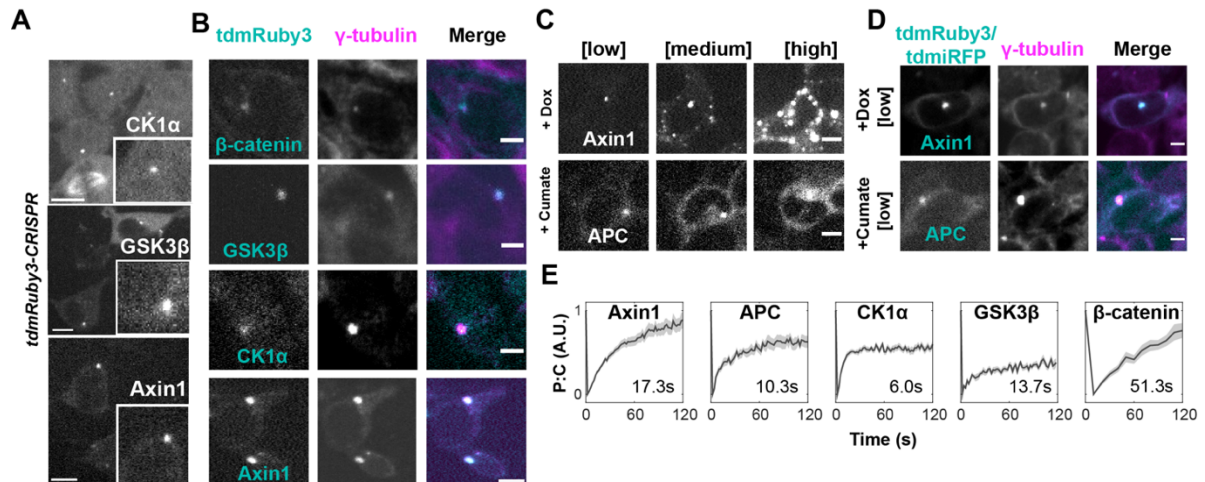
Figure 2.2: Canonical Destruction Complex (DC) components reside in liquid droplets nucleated at the centrosome. A. Representative images of CRISPR-integrated tdmRuby3-CK1α, tdmRuby3-GSK3β and Axin1-tdmRuby3 cells. *Insets*: closeup views of singular peri-nuclear puncta. Scale = 10μm. **B.** Representative cells bearing the indicated DC component fixed and stained for endogenous γ-tubulin. Scale = 10μm. **C.** Representative timelapse images from live cells bearing dox- and cumate-inducible Axin1 and APC cassettes under induction. Montages depict the same cell increasing its DC scaffold concentration through time. **D.** Representative cells bearing the indicated DC component fixed and stained for endogenous γ-tubulin. **E.** Fluorescence recovery after photobleaching (FRAP) traces of mean puncta:cytoplasm fluorescence ratio for indicated DC components. Data presented as mean +/- s.e.m. normalized to extent of bleaching (N=39, 20, 33, 17, 22 for Axin1, APC, CK1α, GSK3β, β-catenin respectively). Individual FRAP traces were fit to the equation: $f(t) = a(1-e^{(-bt)})$ to obtain a and b parameters and half-max recovery time ($\tau 1/2$). Mean $\tau 1/2$ for each DC component is displayed on each plot.

CRISPR to knock in tdmRuby3 into the loci of *CSNK1A1*, *GSK3B,* and *AXIN1*,

genes encoding the kinases CK1α and GSK3β that sequentially phosphorylate β-cat

in the DC, and the primary DC scaffold.

We found that all tagged proteins were localized into 1-2 perinuclear puncta

(**Fig. 2.2A**). Timelapses revealed that the number and position puncta were

determined by cell cycle stage (**Supp. Fig. 2.2A**): we observed single condensates

in G1, two condensates in G2/S, and a "finger-like" pattern—suggesting association

with the mitotic spindle—during late mitosis. These observations, combined with

previous reports of perinuclear enrichment of CK1α, GSK3β and Axin1 in fixed

cells[42–44], led us to hypothesize that these DC components and β-cat were

associated with the centrosome. Immunofluorescence staining for γ-tubulin (**Fig. 2.2B**) and GM130 (**Supp. Fig. 2.2B)** confirmed that tdmRuby3-CK1α, tdmRuby3-GSK3β, and tdmRuby3-β-cat puncta were indeed co-localized to the centrosome.

When overexpressed, Axin and APC cross the phase boundary and form liquid condensates in the cytoplasm that are hypothesized to concentrate DC kinases and β-cat[45]. The fact that no extra-centrosomal DC-puncta were observed in cells at endogenous concentrations led us to hypothesize that the DC is a liquid organelle that is nucleated at the centrosome at endogenous protein concentrations, but forms extra-centrosomal condensates at higher concentrations.To test whether Axin1 and APC are localized to the centrosome at low cellular concentrations, but not when overexpressed, we generated clonal 293Ts bearing doxycycline (Dox)-inducible human Axin1-tdmRuby3 and cumate-inducible human APC-tdmiRFP670. At low levels of induction, both Axin1 and APC localization mirrored CRISPR CK1α, GSK3β, Axin1 and β-cat, forming bright perinuclear puncta (**Fig. 2.2C** *left*) that colocalized with centrosomal markers (**Fig. 2.2D, Supp. Fig. 2.2B)** and replicated following cell cycle progression (**Supp. Fig. 2.2A**). As protein concentration increased, Axin1, but not APC, caused formation of extra-centrosomal puncta throughout the cytoplasm (**Fig. 2.2C-E**). To determine whether extra-centrosomal condensates observed at high Axin1 concentrations were capable of concentrating canonical DC components similar to centrosomal DCs, we next expressed Dox-Axin1-GFP in CRISPR tdmRuby3-CK1α and GSK3β backgrounds. Cells with high Axin1 levels formed extra-centrosomal condensates colocalized with APC, CK1α and β-cat (**Supp Fig. 2.2E**). Interestingly, extra-centrosomal Axin1 condensates did
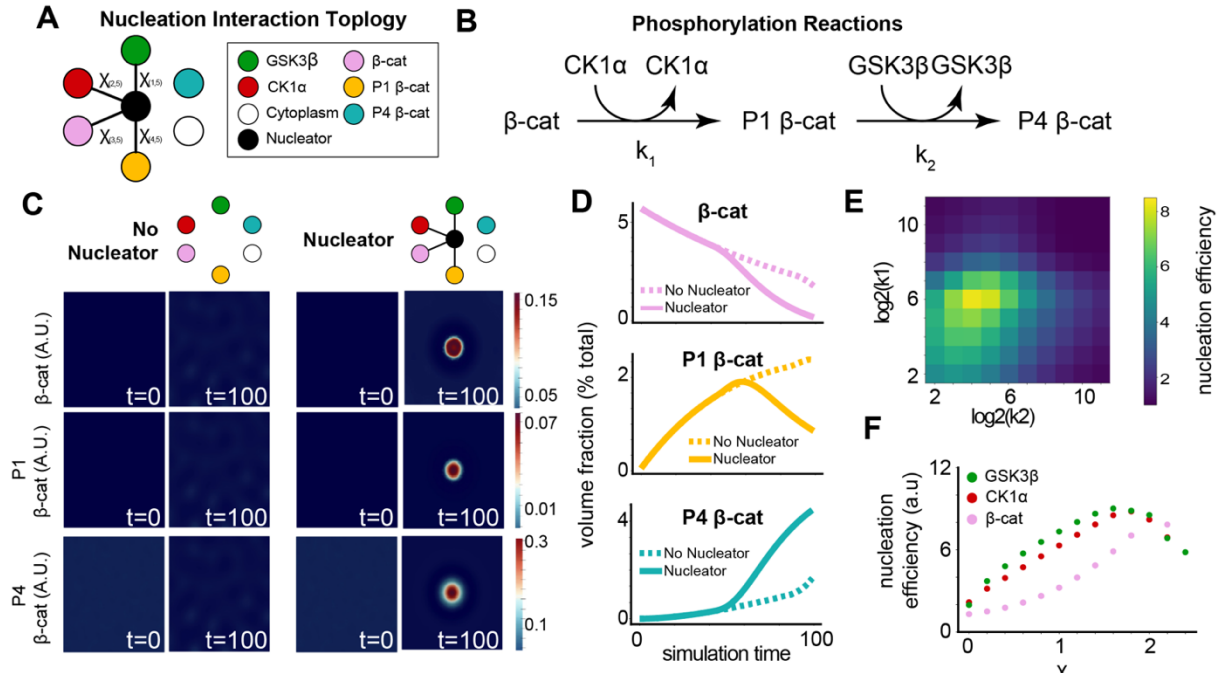
Figure 2.3: *In silico* modelling of β-catenins processing efficiency from a nucleated liquid droplet A. Nucleation interaction topology that describes the interactions between each component of the simulation. Connected components minimize free energy by mixing and unconnected components either de-mix or remain in a non-interacting neutral state. **B.** Schema describing the phosphorylation reactions and rates modeled in the simulation. **C.** Simulation at steps 0 and 100 comparing a system with and without a centrosome. **D.** Quantification of each form of β-catenin with and without a centrosome. **E.** Nucleation efficiency as a function of both rate parameters k_1 and k_2. **F.** Nucleation efficiency in simulations as a function of the interaction parameters between a single client and the cytoplasm.

not reliably induce formation of extra-centrosomal GSK3β condensates in these

experiments, but often resulted in de-enrichment of centrosomal puncta (**Supp. Fig.**

2.2E). We reason that this was due to extra-centrosomal Axin1 condensates

competing for relatively scarce of GSK3β, thereby diluting across all condensates in

the cytoplasm.

293Ts are commonly used in experiments probing DC mesoscale structure *in*

vivo[23,25], but expression of Wnt pathway components may vary significantly between

stem cells and differentiated cells. We observed the same preferential localization of

Axin1 at low concentration in human induced-pluripotent stem cells (iPSCs) (**Supp.**

Fig. 2.2F). These findings establish that all DC components necessary for

phosphorylating β-cat, prior to its ubiquitination, are localized at the centrosome throughout the cell cycle and suggest that DC centrosomal nucleation is generalizable to multiple cell types.

Next, we sought to determine the material state of the centrosomal DC using FRAP on CRISPR-tagged CK1α, GSK3β, and β-cat, as well as of Axin1 and APC at low levels of induction. All centrosomal DC components exhibited mean half-maximal recovery times (τ1/2) between 10 and 60s (**Fig. 2.2E**)—like in over-expressed systems[44] and in-line with mesoscale cellular structures considered liquid-like[46]. Interestingly, relatively wide variation in both stable fraction and τ1/2 was observed between centrosomal DC components, indicating differential turnover of monomers between condensates and the bulk cytoplasm. This suggests that multiple biophysically distinct pools of each component, with different condensation dynamics, co-exist at the centrosome together. Despite this, these results support the idea that the DC is a liquid nucleated by the centrosome and suggest that nucleation has a role in maintenance of cellular β-cat levels.

A reactive Cahn-Hilliard model predicts accelerated b-catenin processing upon centrosomal nucleation of DC clients

To understand the effect of centrosomal nucleation of DC components on β-cat processing, we simulated the processive phosphorylation of β-cat by DC kinases, using a reactive, multi-component, Cahn-Hilliard system[47,48]. We represented the function of DC scaffolds implicitly through the interaction parameters between

kinases and β-cat **(Fig. 2.3A-B, Supp. Fig. 2.3A-D).** Indeed, synthetic DC scaffolds with these simple attributes have been shown to rescue aberrant Wnt signaling[49]**.**

To test the effects of nucleation on β-cat processing, we compared simulations in the presence and absence of a nucleation region (**Fig. 2.3C**). We found that for systems that did not spontaneously phase separate, mimicking the endogenously expressed conditions observed above, DC components localized into a single droplet surrounding the nucleator but did not spontaneously de-mix in its absence **(Supp. Vid 4, 5)**. We found that the nucleated system processed β-cat and its intermediates more quickly (**Fig. 2.3D**) over a wide range of nucleator sizes (**Supp Fig. 2.3E**). See materials and methods for detailed discussion of nucleation parameter scan results. Notably, the nucleated system accelerated β-cat processing, increasing pathway efficiency (**Supp. Fig. 2.3F**). This efficiency gain was maintained over a large range of reaction rates (**Fig. 2.3E, Supp Fig. 2.3G**). As expected, in systems with high reaction rates, the effect of nucleated phase separation is no longer observed.

Given our findings that nucleation drives efficient processing of β-cat, we hypothesized that χ, the interaction parameter that drives phase separation, is a control parameter for β-cat processing. To determine the relationship between DC function and the interaction strength parameter, we systematically decreased the χ between DC clients and the cytoplasm. We found that reducing condensation on the nucleator, through altering χ, decreased the speed and efficiency of β-cat processing (**Supp Fig 2.3H-I**, **Fig. 2.3F, Supp. Vid 6**). Together, these results demonstrate that nucleation of DC components has the potential to increase β-cat

processing and that a tunable control parameter of this process is the free energy of mixing.

Optogenetically-driven enrichment of centrosomal GSK3β condensates rescues hyperactivated Wnt signaling

In silico analysis of the DC indicates that processing efficiency in the presence of a nucleator is dependent on client condensation. Imaging of GSK3β showed relatively weak enrichment in centrosomal puncta compared to CK1α, suggesting that increasing nucleation of GSK3β would increase the degradation rate of β-cat *in vivo.* Changing concentration alters both propensity to
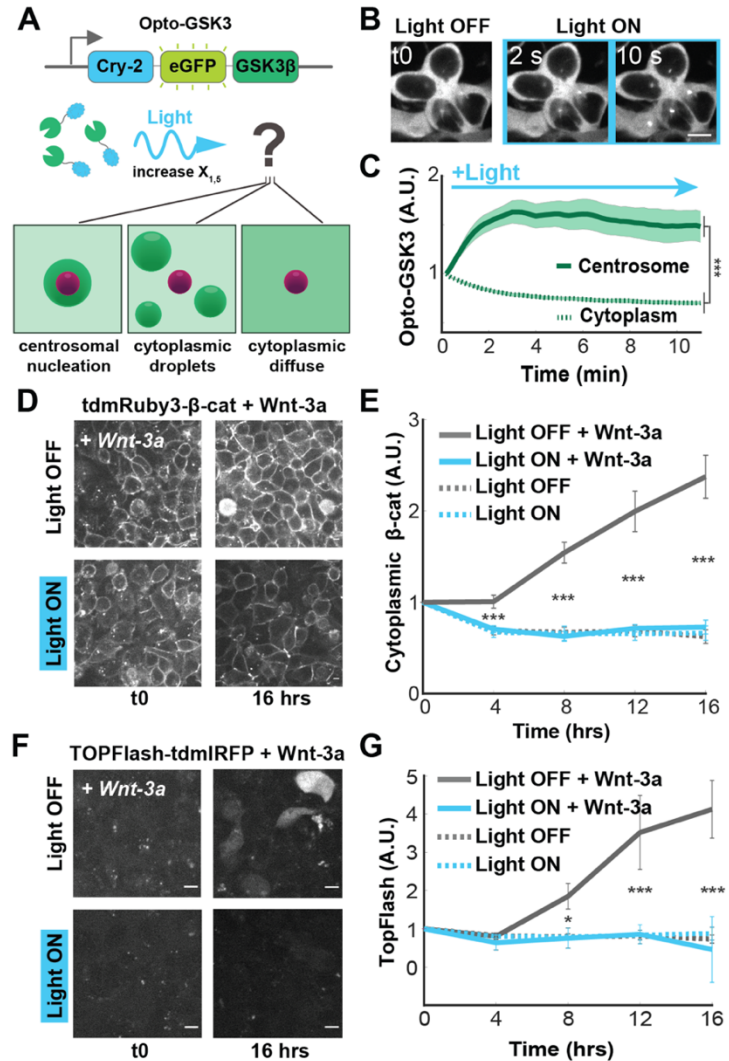
Figure 2.4: Optogenetic clustering of GSK3β increases centrosomal droplet partitioning and suppresses Wnt pathway activation. A. Schematic of Opto-GSK3 and possible spatial outcomes of blue light stimulation. **B.** Representative images of cells bearing Opto-GSK3 responding to blue light stimulation. Montage depicts the same cells throughout the activation timecourse. Scale = 10μm. **C.** Quantification of cells in **B:** Mean fluorescence fold-change from t0 for each compartment +/- s.e.m. (N=20 cells). **D.** Representative images of cells bearing Opto-GSK3 + tdmRuby3-β-catenin following treatment with Wnt-3a. Scale = 10μm. **E.** Quantification of cells in **D:** Mean fluorescence fold-change from t0 +/- s.e.m. is shown (N=20 cells per condition). **F.** Representative images of cells bearing Opto-GSK3 + TOPFlash-IRFP following treatment with Wnt-3a. Scale = 10μm. **G.** Quantification of **F:** Mean fluorescence fold-change from t0 +/- s.e.m. is shown (N=24 cells per condition).

undergo LLPS and reaction rate[28] and therefore cannot be used to test the effect of

nucleation on reaction rate. Optogenetic photo-clustering domains can

independently control intracellular LLPS at fixed concentrations via light-induced

changes in valency between monomers[50,51]. Thus, we reasoned that an optogenetic

tool that drives changes in free energy could isolate the effect of nucleation from

biological function.

To test if photo-clustering increases partitioning to a nucleator, we fused the

photo-oligomerizer Cryptochrome-2 (Cry-2) and eGFP to human GSK3β ("Opto-

GSK3" hereafter) and stably transduced it into 293Ts (**Fig. 2.4A**). Upon light

stimulation, Opto-GSK3 increased its centrosomal enrichment, doubling the mean

centrosome:cytoplasm fluorescence ratio within 10 seconds of activation (**Fig.

2.4B,C, Supp Vid. 7**). Notably, activation of Opto-GSK3 strictly resulted in the

formation of 1 or 2 perinuclear puncta and did not form extra-centrosomal

condensates, contrasting with results from studies using Cry2 alone[50]. Thus, we

found that illumination of Opto-GSK induced condensate formation only at the

centrosome.

To determine whether increased centrosomal condensation of GSK3β

controlled Wnt signal transmission, we activated Opto-GSK3 in cell lines with three

distinct methods for increasing the cellular concentration of β-cat: ligand-induced,

kinase inhibition, and dox-induced gene upregulation. We found that Opto-GSK

activation abolished both Wnt-3a-induced β-cat accumulation and transcriptional

activation as measured by TOPFlash fluorescence (**Fig. 2.4D-E**). Control

experiments comparing cells in light vs. dark confirmed that this was not due to light

alone (**Supp. Fig. 2.4A-B**). We observed a similar effect when analyzing total β-cat

by Western blotting and immunofluorescence staining (**Supp Fig 2.4C-E**). Given the

modest accumulation of β-cat in response to Wnt-3a in 293Ts, we tested to see if

Opto-GSK3 clustering was sufficient to blunt β-cat accumulation induced by either

CHIR or a Dox-inducible β-cat over-expression construct. Indeed, activation of Opto-

GSK3 also inhibited both methods for driving β-cat accumulation in a light-

dependent manner (**Supp Fig 2.4F-J**). These results demonstrate that increasing

DC client nucleation at the centrosome dictates Wnt signal transmission across a

wide range of activation regimes.

Centrosomal enrichment of GSK3β prevents Wnt pathway activation-induced
differentiation of embryonic stem cells

Changes in β-cat
concentration
differentiate a variety
of stem cell
populations, including
human embryonic
stem cells
(hESCs)[50,52]. Having
determined that
increased
centrosomal
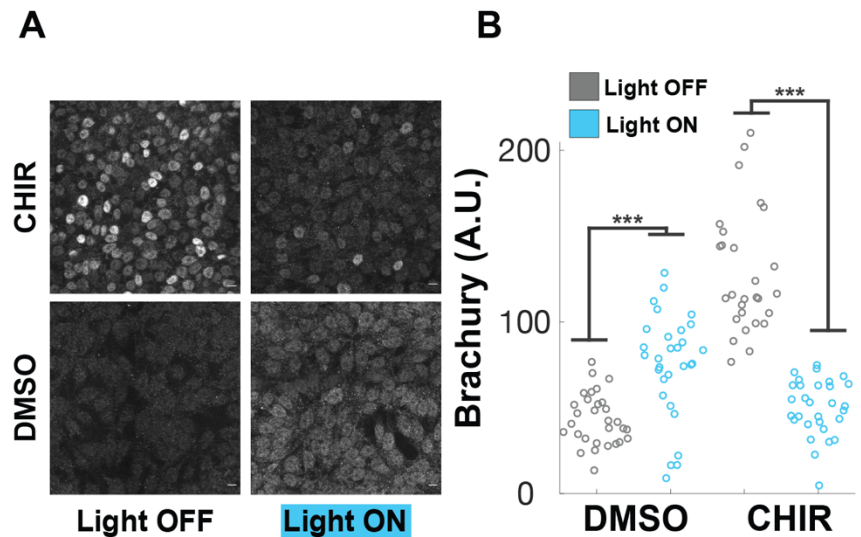
Figure 2.5: Optogenetic clustering of GSK3β suppresses Wnt pathway-mediated differentiation of embryonic stem cells. A. Representative images of H9 embryonic stem cells bearing Opto-GSK3 following 24hrs in described conditions, fixed and stained for endogenous Brachyury. **B.** Quantification of experiment from **A:** Mean nuclear fluorescence for cells measured in each condition is presented.

nucleation of GSK3β is sufficient to reduce β-cat accumulation and Wnt-responsive gene transcription in 293T cells, we wondered whether it was also sufficient to prevent the downstream differentiation of hESCs. Both CHIR and Wnt-3a induce hESC differentiation into mesoderm[53]. To test whether centrosomal nucleation prevents differentiation, we expressed Opto-GSK3 in H9 hESCs and treated them with CHIR or DMSO control in the presence or absence of activating blue light. Following stimulation, cells were fixed and stained for Brachyury (BRA) to assay for differentiation. In the dark, hESCs receiving CHIR responded robustly, displaying bright nuclear BRA compared to DMSO controls (**Fig. 2.5A** *left*). However, when stimulated with blue light, CHIR-treated cells showed significantly reduced levels of BRA staining compared to the dark controls, indicating that nucleation of GSK3b countered CHIR-induced differentiation into mesoderm (**Fig. 2.5A** *right*). Interestingly, we observed that BRA levels in DMSO and light condition were slightly, but significantly, higher than when in the dark, suggesting that over-repression of the Wnt pathway by Opto-GSK3 activation weakly promotes differentiation in hESCs as well (**Fig. 2.5B**).

Discussion

Building on recent discoveries suggesting that LLPS plays a role in DC structure, we sought to understand how the biophysics of DC proteins regulate DC function in live cells. Through a combination of super-resolution microscopy, *in silico* modeling, and optogenetic methods to isolate and probe the phase diagram, we discovered that the mesoscale structure of the DC is a liquid condensate nucleated by the centrosome.

The complementarity of these methods allowed us to identify a function for nucleation: acceleration of the catalytic action of DC proteins, thereby promoting efficient processing of β-cat.

The presence of many cytoplasmic Axin1 and APC droplets in mildly overexpressed cellular conditions[9,53] has been cited in support of the idea that DC scaffolds spontaneously phase separate at endogenous concentrations. Yet, because of the sensitivity of LLPS to concentration, we sought to examine the biophysics of DC components at endogenous concentrations. We found that at low or endogenous levels, all DC components form dynamic assemblies with preferred localization to the centrosome. These results suggest that centrosomal nucleation lowers the concentration threshold for DC condensation.

Our results support a "molecular crucible" model of β-cat degradation, in which multivalent DC scaffolds concentrate DC clients in nucleated droplets to increase β-cat phosphorylation rate. Assembly-line models for β-cat degradation have been proposed[9,54] and Axin1 polymerization has been observed to be ordered *in vitro*[54]. Yet, others have shown that DC condensates display hallmarks of disorder, such as surface tension-minimization, rapid fission/fusion[55], and responsivity to concentration and interaction strength[55,56]. Our results demonstrate that increased multivalency due to optogenetic photoclustering accelerates β-cat degradation, suggesting that DC function is responsive to disordered partitioning of DC clients into condensates.

We found that centrosomal DCs cease to concentrate β-cat under Wnt ON and GSK3β chemical inhibition, but the mechanism for this change remains unclear.

Multiple DC components that bind β-cat--including Axin1, GSK3β and CK1α--are also binding partners of the Frizzled-LRP6 signalosome[56,57], a known inhibitor of GSK3β's phosphorylation of β-cat. Wnt-activated signalosomes may therefore compete with β-cat and/or GSK3β for DC proteins necessary for phosphorylation and degradation, resulting in the accumulation of nascent β-cat in the cytoplasm. For example, GSK3β phosphorylation is known to regulate APC's R2/B motif which is critical for APC/Axin interaction and β-cat degradation[44]. Alternatively, Dvl was recently found to regulate Wnt pathway activation via its affinity for Axin1's DIX domain[36], potentially 'invading' and destabilizing Axin-Axin multimerization; such invasion of the DC could dilute Axin1 and its associated clients in the DC, reducing the phosphorylation rate of β-cat.

Our results raise an important question that may lead to the discovery of unknown potentiators of Wnt signal transduction: what is/are the nucleator(s) coupling the DC to the centrosome? Axin1 is known to associate with γ-tubulin[37,55] and is a substrate of PLK1, a kinase involved in centrosome duplication during cell cycle progression[37,57], suggesting that it is redundantly associated with the centrosome. APC is a regulator of microtubule stability and growth[37,58], and its armadillo repeat region is sufficient to induce centrosomal localization[58,59]. Multiple binding sites for DC scaffolds could localize the DC to the centrosome, increasing the robustness of droplet nucleation and enriching local client concentration. Notably, elimination of centrioles in developing mice and *drosophila* embryos leads to only minor tissue-level defects in canonical Wnt signaling and overall morphology[59,60], indicating that centrosomes are not essential for Wnt-mediated

embryogenesis. We show that Axin is critically poised at the phase boundary so it is possible that DC condensation is restored via simple upregulation of this scaffold or the presentation of another nucleator through feedback mechanisms. Alternatively, another undiscovered DC nucleator that normally localizes to the centrosome may be sufficient to drive DC condensation when the centrosome is absent.

Finally, centrosomal nucleation of the DC suggests a potential function in coordinating cell cycle progression with Wnt signaling. We found two DC droplets in cells with duplicated centrosomes, suggesting that the DC is split along with centrosomes during mitosis. Non-nucleated droplets would be randomly partitioned into daughter cells, leading to potentially detrimental asymmetry in Wnt signaling capacity of the growing tissue. Cell cycle synchronization could be a method of reducing heterogeneity in Wnt-induced stem cell differentiations.

Overall, our studies suggest an integral role for LLPS nucleation in regulating the activity of membraneless organelles *in vivo*. The power of observing proteins in their endogenous contexts, coupled with the ability to precisely tune interaction strength without altering protein function or concentration, enables the functional dissection of membraneless organelles.

Materials and Methods

Cell Lines. Human 293T cells were cultured at 37°C and 5% CO2 Dulbecco's

Modified Eagle Medium, high glucose GlutaMAX (Thermo Fisher Scientific,

10566016) medium supplemented with 10% fetal bovine serum (Atlas Biologicals, F-

0500-D) and 1% penicillin-streptomycin. Human induced pluripotent stem cell line

(hiPSC) WTC was gifted by the Pruitt lab (purchased from Coriell). hiPSCs were

propagated on Matrigel® coated tissue culture plates using serum-free essential 8

(Gibco) culture conditions in standard environments consisting of 5% carbon dioxide

at 37°C. Experiments in human Embryonic Stem Cell (hESC) lines were performed

using the H9 hESC cell line purchased from the William K. Bowes Center for Stem

Cell Biology and Engineering at UCSB. Cells were grown in mTeSR™ Plus medium

(Stem Cell Technologies) on Matrigel® (Corning) coated tissue culture dishes and

tested for mycoplasma in 2-month intervals.

Cloning of PiggyBac Transposase and Lentiviral Overexpression Constructs.

pPig_H2B-mTagBFP2::t2A::Cas9-Avidin was constructed via subcloning human

H2B, mTagBFP2 and Cas9-Avidin provided by Max Wilson into an expression vector

bearing a CMV promoter and flanking PiggyBac transposase-compatible inverted

terminal repeats using Gibson Assembly (New England BioLabs Inc., E2611L)

according to supplier instructions. Each of the PCR fragments used were amplified

using the following primers:

PiggyBac (CMV) Backbone fwd: tgacgcccgcccccac rev: ggtaagcttttgcaaaagcctaggcc.

H2B + 18AA linker fwd: cctaggcttttgcaaaaagcttaccatgccagagccagcgaagtc rev:

GCATATTTTCCTTGATGAGTTCACTCATccCagTatGtcCgcCggAg. mTagBFP2 fwd:

ATGAGTGAACTCATCAAGGAAAATATGCACATG rev:

CGTCCCCGCAGGTCAACAAACTTCCGCGACCTTCTCCGCTCCCATTGAGCTTAT

GGCCGAGTTTGCTG. 3X-Flag-NLS-Cas9-HA-Avidin fwd:

GGAAGTTTGTTGACCTGCGGGGACGTGGAAGAAACCCGGGTCCAgactataagga

ccacgacggagactac rev: gctgcgggtcgtggggcgggcgtcaggatccagacgccgcag

XLone-Axin-tdmRuby3 was constructed via PCR and Gibson Assembly, subcloning

from the following constructs: Flag-Axin1 purchased from Addgene (#109370),

tdmRuby3 from Max Wilson into XLone-GFP purchased from Addgene (#96930)

containing 3rd gen tet ON-responsive promoter and EF1α-driven Blasticidin selection

cassette. The following primers were used: XLone Backbone fwd:

taaactagtagaccacctcccctgcg, rev: ggtacctttacgagggtaggaagtgg, human Axin1 fwd:

cacttcctaccctcgtaaaggtaccatgaatatccaagagcagggtttcccc, rev:

CCATgctTCCgCCgCCACTACCgCCgtccaccttctccactttgccgatgatc, 7AA link-

tdmRuby3 fwd: GGcGGTAGTGGcGGcGGAagcATGGTTAGCAAAGGGGAGGAGC,

rev: gcaggggaggtggtctactagtttaCTTGTACAGCTCGTCCATGCCG.

XLone-bCat-tdmRuby3 was constructed via PCR and Gibson Assembly, subcloning

from the following constructs: XLone-Axin-tdmRuby3 (above) and Human Beta-

catenin GFP purchased from Addgene (#71367). The following primers were used:

XLone Backbone fwd:

GGcGGTAGTGGcGGcGGAagcATGGTTAGCAAAGGGGAGGAGC, rev:

ggtacctttacgagggtaggaagtgg, human bcat fwd:

29

cacttcctaccctcgtaaaggtaccatggctactcaagctgatttgatggagttg, rev:

CCATgctTCCgCCgCCACTACCgCCcaggtcagtatcaaaccaggccagc

pPig_CuO-APC-tdmIRFP670::CymR was constructed via PCR and Gibson

Assembly from the following constructs: pCuo CA Rac1 CMV + cumate operon

purchased from Addgene (#84643), human APC open reading frame purchased

from Addgene (#16507), tdmirfp670nano from Max Wilson, human ubiquitin C-driven

CymR Cuo repressor purchased from Addgene (#119907) into pPig-Hygro

transposase backbone from Max Wilson. PCR fragments were amplified using the

following primers:

pPig-Hygro Backbone fwd:

GGACGTGGAAGAAACCCGGGTCCAatgggtaaaaagcctgaactcaccgc, rev:

cattccacagggtcgacagtacaagc,

Cuo + CMV fwd: cttgtactgtcgaccctgtggaatgcgttacataacttacggtaaatggcccgc,

rev: actgatcatatgaagctgcagccatgaattcggtaccggatccagtcgactag,

APC fwd: atggctgcagcttcatatgatcagttgttaaagcaag,

rev: CCATgctTCCgCCgCCACTACCgCCaacagatgtcacaaggtaagacccagaatg,

7AAlinker-tdmirfp670nano fwd: GGcGGTAGTGGcGGc,

rev: ggcgccaaaacccggcgcggaggccttaGGACTGCTGTATTGCAATGCCAACTAC,

UbC-CymR-V5-T2A fwd: ggcctccgcgccggg,

rev:

TGGACCCGGGTTTTCTTCCACGTCCCCGCAGGTCAACAAACTTCCGCGACCTT

CTCCGCTCCCcgtagaatcgagaccgaggagagg

pLV_Cry2-tdeGFP-GSK3b was obtained via synthesis and cloning services provided by Vector Builder Inc. Full details available upon request, but briefly: primary plasmids containing *Arabadopsis thaliana*, tdmIRFP from Max Wilson and human GSK3β purchased from Addgene (# 16260) ORFs were supplied to VectorBuilder for cloning and EF1α-driven expression into 3rd generation lentiviral backbone. Vectorbuilder provided the desired final, sequenced plasmid.

pPig_8XTOP_tdIRFP_Puro was constructed via PCR and Gibson Assembly from the following constructs: pPig_H2B-mTagBFP2::t2A::Cas9-Avidin (above), M50 Super 8x TOPFlash purchased from Addgene (#12456) and codon-optimized tandem (td)IRFP ordered from Twist Biosciences as overlapping gene fragments with the sequences:

ATGGCTGAAGGCAGCGTGGCCCGACAGCCAGACCTTTTGACTTGTGACGATGA

ACCAATCCACATACCGGGGGCAATACAACCTCATGGTCTCCTTCTGGCGCTTG

CTGCCGACATGACTATAGTGGCCGGCTCTGACAACTTGCCGGAATTGACCGGA

CTTGCTATTGGGGCGTTGATTGGGCGCTCTGCCGCTGATGTATTTGATTCCGA

GACACATAATAGGCTTACTATAGCCCTCGCCGAACCAGGGGCTGCCGTCGGCG

CTCCTATAACAGTTGGGTTCACGATGCGAAAAGATGCTGGGTTCATTGGTAGCT

GGCATCGCCACGATCAACTTATCTTCCTTGAGCTTGAACCCCCTCAACGGGAC

GTTGCGGAACCCCAAGCTTTCTTTAGAAGGACCAATTCAGCCATAAGGCGCCTT

CAGGCCGCAGAGACATTGGAGTCCGCGTGTGCGGCAGCAGCGCAGGAAGTAC

GAAAGATCACGGGATTTGACCGGGTTATGATTTACAGATTCGCATCTGATTTCT

CCGGGGAAGTCATCGCGGAGGATCGGTGTGCAGAAGTGGAAAGCAAGCTTGG

TTTGCATTACCCCGCATCTACGGTTCCGGCCCAAGCGAGGAGACTGTATACGA

31

TAAACCCAGTGAGGATCATACCTGACATAAATTATAGACCGGTTCCCGTTACGC

CAGACCTGAACCCCGTCACAGGCAGGCCAATAGACTTGTCTTTTGCAATCCTG

CGGTCAGTCTCACCTGTTCACCTCGAGTTTATGAGGAACATAGGGATGCATGG

GACGATGAGCATCTCAATCCTGAGAGGTGAACGGCTCTGGGGACTTATTGTTT

GTCATCATCGCACACCGTATTACGTTGACCTTGATGGTCGCCAGGCCTGCGAA

CTCGTAGCTCAAGTATTGGCCTGGCAGATCGGTGTTATGGAGGAAAGCGGTCA

TGGGACTGGGAGTACAGGTAGCGGCAGCTCTAGTGGCACCTCC

and

TAGCGGCAGCTCTAGTGGCACCTCCATGGCAGAAGGGTCCGTAGCAAGGCAA

CCTGACTTGTTGACCTGTGATGATGAACCGATTCACATTCCTGGAGCAATTCAA

CCGCATGGGCTGCTCCTTGCTTTGGCAGCGGACATGACGATCGTCGCCGGCT

CCGATAACCTGCCCGAGTTGACGGGCTTGGCGATAGGAGCCCTGATAGGCCG

CTCAGCCGCTGACGTATTCGATAGCGAAACGCATAACCGGCTTACAATCGCCT

TGGCTGAACCGGGCGCGGCCGTGGGAGCACCGATTACTGTAGGCTTTACAAT

GAGAAAAGACGCCGGCTTTATCGGGTCATGGCACCGACATGACCAGCTGATTT

TCCTGGAATTGGAGCCCCGCAGCGGGATGTAGCCGAACCACAGGCCTTCTTC

CGGCGCACTAACTCCGCAATTAGGAGACTGCAGGCAGCTGAGACTTTGGAATC

AGCATGCGCGGCAGCTGCACAAGAAGTCCGGAAAATCACGGGTTTTGACCGA

GTCATGATCTATAGATTCGCGAGCGATTTCTCAGGAGAAGTTATTGCGGAAGAC

CGATGCGCGGAGGTAGAATCTAAGCTTGGGTTGCACTACCCCGCCTCCACCGT

TCCGGCGCAAGCCAGACGGCTCTATACCATTAATCCGGTGCGGATCATTCCAG

ATATAAATTACCGGCCTGTACCTGTGACACCGGATTTGAACCCTGTCACGGGC

CGACCGATAGACCTCAGCTTCGCTATATTGCGATCTGTGTCACCGGTCCACCTC

GAGTTTATGAGGAATATAGGCATGCATGGTACAATGTCCATTTCCATTCTCCGG

GGTGAACGGCTTTGGGGCCTCATCGTTTGTCACCATCGAACACCGTATTACGT

CGATCTCGACGGCAGACAGGCATGTGAGTTGGTCGCTCAGGTACTCGCTTGGC

AGATAGGGGTAATGGAGGAG

PCR fragments were amplified using the following primers:

PiggyBacPuro backbone fwd:

ACCTGCGGGGACGTGGAAGAAACCCGGGTCCAatgaccgagtacaagcccacggtg,

rev: cattccacagggtcgacagtacaagcaaaaag.

8X TOPFlash fwd: cttgtactgtcgaccctgtggaatgaagtgcaggtgccagaacatttctc,

rev: GTCGGGCCACGCTGCCTTCAGCCATggtggctttaccaacagtaccgg.

tdIRFP1 fwd: ATGGCTGAAGGCAGCGTGGC,

rev: GGAGGTGCCACTAGAGCTGC. tdIRFP2

fwd: TAGCGGCAGCTCTAGTGGCAC,

rev:

GGTTTTCTTCCACGTCCCCGCAGGTCAACAAACTTCCGCGACCTTCTCCGCTCC

CCTCCTCCATTACCCCTATCTGCCAAGCG.

All above constructs were transformed into Top10 competent cells prepared using

Mix & Go E.coli Transformation Kit and Buffer set (Zymo Research #T3002),

cultured on LB agar plates to select for antibiotic resistance using standard

workflows for molecular cloning and DNA production[61]. Plasmid DNA was purified

using the Zyppy Plasmid Miniprep kit (Zymo Research #D0436). In addition to

antibiotic selection, constructs were verified via Sanger sequencing using primers

targeting fusion junctions of relevant construct domains.

Lentiviral Production and Transduction. Production of lentivirus carrying opto-GSK3 was accomplished via co-transfection of pLV_Cry2-tdeGFP-GSK3b, pCMV dR8.91 (obtained from Jared Toettcher's Lab at Princeton University) and pMD 2.G at a 1: 0.88 : 0.11 *mass* ratio using standard PEI-based transfection procedures[62] Cells were incubated for 24 hours before replacing with fresh media and allowing for lentiviral production for an additional 48 hours. Supernatant was harvested, filtered through 0.22um filter and added to plated cells for transduction. *NOTE: All steps for lentiviral production, transduction and subsequent maintenance of cell lines were carried out in the presence of far-red light or the complete absence of light in attempt to eliminate the possibility of Cry-2 opto-GSK3 clustering interference with cell growth or virus production.

Construction of CRISPR gRNA Constructs and Homology-Directed Repair Templates. Genomic edits in 293Ts were carried out in cells constitutively expressing Cas9 to maximize editing efficiency.

pCAB_minimal gRNA backbone: A vector expressing guide RNA and Cas9 obtained from Max Wilson was subcloned to remove the unnecessary Cas9 ORF via PCR using the following primers:

fwd: acgcgccctgtagcg

rev: cttaatgcgccgctacagggcgcgtggtacctctagagccatttgtctgc,

assembled, cloned, purified and verified as described in the previous section. The baseline pCab_minimal construct was then subsequently used for production of

gRNAs targeting exon1 of the human genomic loci of CTNNB1, CSNK1a1, GSK3B. Primers creating 1-3 (depending on PAM site availability/predicted on/off-target editing scores) unique protospacers targeting the 50-bp window surrounding the 1st codon of each gene were annealed and cloned into the pCAB_minimal via BbsI digestion and ligation (New England BioLabs # R3539S, Takara #6023) using standard protocols[63]. The following primers were used for sticky-end ligation of protospacers:

CTNNB1_1 fwd: caccgTGAGTAGCCATTGTCCACGC rev: aaacGCGTGGACAATGGCTACTCA

CTNNB1_2 fwd: caccgTGAAAATCCAGCGTGGACAA rev: aaacTTGTCCACGCTGGATTTTCAc

CTNNB1_3 fwd: caccGCGTGGACAATGGCTACTCA rev: aaacTGAGTAGCCATTGTCCACGC

CSNK1a1_1 fwd: caccGGCCAAGCCCCGACACCTCT rev: aaacAGAGGTGTCGGGGCTTGGCC

CSNK1a1_2 fwd: caccgAGGCTGAATTCATTGTCGGA rev: aaacTCCGACAATGAATTCAGCCT

GSK3B fwd: caccCGAAGAGAGTGATCATGTCA rev: aaacTGACATGATCACTCTCTTCG

AXIN1 gRNAs were ordered complete from IDT. 4 different protospacer sequences were used (in separate reactions) with the same HDR template to maximize chance

of target locus cutting. Cells from each reaction were then pooled 7 days after

transfection and subsequently enriched together.

Protospacer sequences:

AXIN1_1: GGCCGTCCTGCCCGTCTTTG

AXIN1_2: GTCTTTGAGGAGAAGATCAT

AXIN1_3: gTCTTTGAGGAGAAGATCATC

AXIN1_4: GGAGAAGATCATCGGCAAAG

Homology-Directed Repair (HDR) Templates: Blunt-end PCR products were used in

conjunction with gRNAs to template genomic edits containing desired knock-ins.

Blunt-end, double-stranded HDR templates were created via DNeasy Blood and

Tissue genomic prep kit (Qiagen, 69504) of 293T cell line to be edited (see next

section) and PCR using primers targeting amplicons of a 500-1000bp window

centered on the intended cut site. The following primers were used to amplify

genomic loci homology regions:

tdmRuby3:

GGcGGTAGTGGcGGcGGAagcATGGTTAGCAAAGGGGAGGAGCTTATAAAGGAA

AATATGAGAATGAAAGTTGTCATGGAAGGTTCAGTGAATGGCCATCAGTTTAAA

TGTACAGGTGAAGGCGAGGGACGCCCTTATGAAGGAGTCCAAACTATGAGGAT

CAAAGTCATAGAGGGAGGTCCTCTCCCCTTCGCCTTCGATATCCTCGCCACCT

CTTTCATGTATGGTTCAAGAACATTTATCAAGTATCCTGCCGATATACCAGACTT

CTTTAAGCAGTCATTTCCAGAAGGTTTCACTTGGGAACGAGTCACTAGGTATGA

GGACGGCGGGGTTGTGACAGTAACTCAAGACACCTCTTTGGAAGATGGTGAGT

TGGTCTACAACGTGAAGGTACGCGGGGTTAATTTCCCTTCTAACGGGCCTGTTA

TGCAAAAGAAGACAAAGGGTTGGGAGCCAAATACCGAGATGATGTATCCTGCA

GATGGTGGCCTGCGGGGCTATACCGACATCGCTCTGAAGGTAGACGGCGGGG

GCCACCTCCATTGTAATTTTGTAACCACTTACAGGTCTAAGAAGACCGTGGGTA

ACATTAAGATGCCAGGGGTTCATGCTGTCGACCATAGATTGGAGCGGATAGAA

GAAAGCGACAACGAGACCTACGTCGTGCAACGCGAAGTCGCAGTAGCCAAGTA

TTCCAATCTCGGGGGAGGTATGGATGAACTCTATAAAGGCGGATCCGGTGGTG

TGTCCAAGGGAGAAGAACTGATCAAAGAGAACATGAGGATGAAGGTCGTGATG

GAGGGCAGCGTCAACGGACACCAATTCAAGTGCACCGGAGAGGGAGAAGGCA

GACCATACGAGGGCGTGCAGACAATGAGAATTAAGGTGATCGAAGGCGGACC

ACTGCCTTTTGCTTTCGACATTCTGGCTACAAGCTTCATGTACGGCAGCAGGAC

CTTCATTAAATACCCCGCTGACATCCCTGATTTTTTCAAACAAAGCTTCCCTGAG

GGCTTTACCTGGGAGAGAGTGACAAGATACGAAGACGGAGGCGTCGTCACCG

TCACACAGGATACAAGCCTGGAGGACGGAGAACTGGTGTATAACGTCAAAGTC

AGAGGAGTGAACTTTCCCAGCAATGGCCCCGTGATGCAGAAAAAGACCAAAGG

CTGGGAACCTAACACAGAAATGATGTACCCAGCCGACGGAGGACTGAGAGGAT

ACACAGACATTGCCCTCAAAGTGGATGGAGGAGGACATCTGCACTGCAACTTC

GTCACAACCTACAGATCCAAGAAAACAGTCGGAAATATCAAGATGCCTGGCGT

GCACGCCGTGGATCACAGGCTGGAAAGGATTGAGGAGTCCGATAATGAAACAT

ATGTGGTCCAGAGGGAGGTGGCCGTCGCTAAATACAGCAACCTGGGCGGCGG

CATGGACGAGCTGTACAAGGGGGGATCAGGAGGaGGctct

CTNNB1 fwd:

ATAAAAAGACATTTTTGGTAAGGAGGAGTTTTCACTGAAGTTCAGCAGTGATGG
AGCTGTGGTTGAGGTGTCTGGAGGAGACCATGAGGTCTGCGTTTCA
CTAACCTGGTAAAAGAGGATATGGGTTTTTTTTGTGGGTGTAATAGTGACATTTA
ACAGGTATCCCAGTGACTTAGGAGTATTAATCAAGCTAAATTTAAATCCTAATGA
CTTTTGATTAACTTTTTTTAGGGTATTTGAAGTATACCATACAACTGTTTTGAAAA
TCCAGCGTGGACAGGcGGTAGTGGcGGcGGAagc

rev:

TAGGGAACCACCTAACAGTTACTCACTGAATCAGTGGAAGAATGGTACTGCATC
CAGGCTCCAGAAGCAGTCATCCAGACTAGATTCCTGCTGGTGGCTT
GTTTGCTATTTCACCAAGCCATTAGGAGGAGTGAGCAGAAAATGGAGCAAAAG
GTAGCCTGACAAGTAAGCAGGGAGAGAGGAAAGCAGGGGGATCTCAGCCAGA
CTGGCTTAATGGCAACGAAGCAGAGCCCCAATTCAGTAACTAAAGATTTAATGA
CACAAACCTTGAGTAGCCATagagCCtCCTCCTGATCCCCC

*NOTE: CTNNB1 homology arms were synthesized (requiring no genomic
amplification step) and provided as a generous gift from Integrated DNA
Technologies.

CSNK1a1fwd: CCAGCCCGCGACGTC rev: CTTGACCCTTTTAGGGAGACAGCG

GSK3B fwd: GATTTGCCCTCTCTTTTCTCTCCTCC rev:
CCAAATAAATATCATATTATCTCAATTCAAGGTTAATGAGACCG

The above amplicons were then used in a second round of PCR to obtain separate

upstream and downstream homology arms that flanked desired knock-ins and

overlap extension was used to construct the final desired amplicons bearing

tdmRuby3 and 7AA GS linker. The following primers were used:

Generic tdmRuby3 insert fwd:

GGcGGTAGTGGcGGcGGAagcATGGTTAGCAAAGGGGAGGAGC, rev:

agagCCtCCTCCTGATCCCCCCTTGTACAGCTCGTCCATGCC

CSNK1a1 upstream homology arm rev:

gctTCCgCCgCCACTACCgCCCCTGAGAGACGAAGATGGAGGC

CSNK1a1 downstream homology arm fwd:

GGGGGATCAGGAGGaGGctctATGGCGAGTAGCAGCGGC

GSK3B upstream homology arm rev:

gctTCCgCCgCCACTACCgCCGATCACTCTCTTCGCGAATCACC

GSK3B downstream homology arm fwd:

GGGGGATCAGGAGGaGGctctATGTCAGGGCGGCCC

AXIN1 upstream homology arm fwd: CTTCACCCACATGTGGTCATTGCAC

AXIN1 upstream homology arm rev:

CGGCAAAGTGGAGAAGGTGGACGGcGGTAGTGGcGGcGGAagc

AXIN1 downstream homology arm fwd:

GGGGGATCAGGAGGaGGctctTGATAGGCTGGTGGGCTGGCC

AXIN1 downstream homology arm rev: CACCTGAAGCTGGCAGCAGG

*NOTE: Original upstream fwd and downstream rev primers listed above for isolating

genomic loci were reused in the present step and thus not repeated here.

CRISPR-Cas9 Fluorescent Tagging. Bare 293T cells were first co-transfected using PEI[62] with the H2B-mTagBFP2 vector and Super PiggyBac Transposase-expressing vector (System Biosciences Inc. # PB210PA-1) via polyethylenimine (Sigma #408727-100mL) transfection reagent and standard workflows[62]. Cells were allowed 72 hours following transfection to reach steady-state expression of integrated construct and were enriched via 2 rounds of fluorescence-activated cell sorting (FACS, SH800S, Sony Biotechnology) for cells fluorescent in the 450nm excitation (blue) channel: a bulk enrichment to obtain a largely 'positive' population and a 2nd to obtain clonal populations. A high-expressing clone was expanded and used as a 'chassis' cell line for subsequent CRISPR editing.

CRISPR chassis cells were then co-transfected with one of the constructed gRNA plasmids and respective HDR templates at a 2:1 HDR template:gRNA plasmid molar ratio and allowed 72 hours to reach steady-state expression. Similar to the process described above, cells were subject to 2 rounds of FACS (561nm excitation, red laser) to obtain a clonal population. Knock-in validation was accomplished via a combination of fluorescence microscopy, genomic PCR and sequencing (using primers for initial amplification of loci and construction of HDR templates). In the case of all intended knock-ins, spatiotemporal fluorescence expression of cell populations was binary (either fluorescent or not) and uniform (no detected variation in brightness or localization between fluorescent clones), suggesting that selected clones were broadly representative of overall edited populations.

Development of Inducible Axin1, APC and β-catenin Cell Lines. 293Ts were co-transfected as described in the previous section with PiggyBac and compatible XLone-Axin-tdmRuby3 and pPig_CuO-APC-tdmIRFP670::CymR expression cassettes. 72 hours following transfection cells were selected in 1uM Blasticidin (Invivogen, #ant-bl-05) and 100ug/mL Hygromycin B Gold (Invivogen, #ant-hg-1). Blast+/Hygro+ cells were then clonally sorted via FACS as described in the previous section to obtain a uniform population for experiments. For iPSCs, Both Piggyback and Donor plasmids were chemically transfected when cells reached 30% confluency using Lipofectamine™ Stem Transfection Reagent (manufactures protocol). Following transfection Blasticidin selection (1uM) was initiated 5 days later. At the end of Blasticidin selection, 12 clones were manually picked under a dissection microscope and continuously cultured in Blasticidin (1uM) for an additional week. Upon fluorescence signal confirming successful integration, Blasticidin (1uM) treatment ceased and 1 clone was chosen for the remaining experiments.

Small Molecules. CHIR 99021 (STEMCELL TECHNOLOGIES # 72052) was resuspended in dimethyl sulfoxide according to supplied manufacturer recommendations and diluted to 5X concentrated stocks in culture medium immediately prior to use on cells. In all cases CHIR was used at 10uM. Doxycycline hyclate (Sigma Aldrich # D9891-1G) was resuspended in phosphate-buffered saline and diluted to 5X desired concentration in culture medium prior to use. Stock cumate

solution (System Biosciences # QM100A-1) was diluted to 5X in culture medium prior to use.

"Low" dose of Dox referred to in **Fig. 2C,D** in the context of Axin and APC induction was 20ng/mL concentration in culture medium, "High" dose was 200ng/mL. "Low" dose of Cumate was 100ng/mL, "High" was 1mg/mL. The dose of Dox used in β-cat induction in **Supp. Fig. 4I,J** was 100ng/mL.

Wnt-3a treatments. Recombinant Human Wnt-3a (R&D Systems 5036-WN-010) was resuspended in in PBS containing 0.1% BSA according to supplied manufacturer recommendations and diluted to 5X concentration in culture medium immediately prior to use. In all cases Wnt-3a was used at a final concentration of 1ug/mL.

Antibodies, Immunofluorescence and Western Blot. Primary antibodies used for immunofluorescent markers of the centrosome were α-GM130 (BD 610822, 1:1000 dil.) and α-γ-tubulin (Sigma Aldrich T5326-25UL, 1:1000). Secondary used for both stains was α-Ms-Alexa-488 (Invitrogen A28175, 1:1000). Tissue fixation and staining was carried out using standard protocols using cold methanol[64] Immunofluorescent samples were imaged using confocal microscopy (see below). Antibodies used for Western Blotting and immunofluorescence were α-β-catenin (Cell Signaling, # 2698S, 1:1000) and α-β-actin (Sigma, A3853, 1:1000). Secondary antibodies used were α-Gt-680RD and α-Ms-800CW (Licor 926-6807 and 926-32212 respectively, both 1:10,000 dil.). Standard immunoblot procedures were used[65].

Imaging. All live and fixed cell imaging experiments were carried out using a Nikon

W2 SoRa spinning-disk confocal microscope equipped with incubation chamber

maintaining cells at 37°C and 5% CO_2. Glass-bottom culture plates (Cellvis # P96-

1.5H-N) were pre-treated with bovine fibronectin (Sigma #F1141) in the case of

293Ts or Matrigel in the case of H9 and iPSCs, and cells were allowed to adhere to

the plate before subsequent treatment or imaging. Fluorescence recovery after

photobleaching was performed via custom Nikon NIS Elements JOBs function and

488nm FRAP laser (Nikon LUN-F laser unit, 100mW power output from the APC

fiber tip).

Optogenetic Stimulation. Spatial patterning of light during timelapse fluorescent

imaging sessions was accomplished via purpose-built microscope-mounted LED-

coupled digital micromirror devices (DMDs) triggered via Nikon NIS Elements

software. Stimulation parameters (brightness levels, duration, pulse frequency) were

optimized to minimize phototoxicity while maintaining continuous activation of Cry-2.

For DMD-based stimulation on the microscope, the final settings for 'Light ON' were

25% LED power (λ = 455nm), 2s duration pulses every 30s. For experiments that did

not require frequent confocal imaging, cells were stimulated via a benchtop LED

array purpose-built for light delivery to cells in standard tissue culture plates

('OptoPlate') adapted from previously established designs[66]. The same light delivery

parameters were used for OptoPlate based stimulation as for microscope mounted

DMDs. Light was patterned to cover the entire surface of intended wells of plates

used, rather than a single microscope imaging field.

Image Analysis. All quantification of raw microscopy images was carried out using the same general workflow: background subtraction > classification > measurement > normalization > statistical comparison. Subcellular segmentation of nuclear fluorescence was performed via custom Matlab scripts using H2B-mTagBFP2 brightness, size and circularity to mask objects. When experimental conditions did not permit segmentation via H2B-mTagBFP2 nuclear fluorescence (such as with live-cell optogenetic stimulation) cells were selected at random using custom ImageJ macro that generates random ROIs (available upon request). Unless otherwise noted, mean fluorescent intensity of regions of interest were measured and subsequently processed. Raw measurements were compiled, processed, and plotted via custom Matlab scripts, available upon request.

Statistical Analysis.

p value range	Symbol
$0.01 < p < 0.05$	*
$0.001 < p < 0.01$	**
$p < 0.001$	***

Table 2.1: All statistical tests were carried out on final grouped datapoints presented in figures using independent samples t-tests (Matlab function "ttest2") except for **Supp. Fig. 4D** which was the result of one-way ANOVAs.

Simulation Methods

We used the python-based FEniCS computing environment (https://fenicsproject.org/) to solve the modified Cahn-Hilliard partial differential equations using the Finite Element Method (FEM). In our simulation, we represent the volume fraction of each DC protein, ϕ_i, as an incompressible volume such that $\sum_{i=1}^{N} \phi_i = 1$ and approximate the reaction rates with spatially dependent analogues to well-mixed reactions using the simplified, non-state dependent description of the second order rate $R_i = k_{i,j}\phi_i\phi_j$, with production and consumption denoted by the sign of $k_{i,j}$[67,68]. The Cahn-Hilliard equation, in its general form, is a parabolic equation with first-order time derivatives, and second- and fourth-order spatial derivatives. To solve this equation using a standard Lagrange finite element basis the equation is recast as two coupled second-order equations:

$$\frac{\partial \phi_i}{\partial t} = \nabla \cdot M\big(\nabla(\mu_i)\big) + R_i\big(k_{i,j}, \phi_i, \phi_j\big)$$

$$\mu_i = \frac{\partial F}{\partial \phi_i} - \lambda \nabla^2 \phi_i$$

Where M_i is the mobility constant, with all DC components having the same diffusion rate, λ is the surface energy parameter that dictates the length of transition regions

between domains, and F is the polynomial double-well description of the free energy:

$$F = \sum_{i=1}^{N-1} \sum_{j=2}^{N} \chi_{i,j} \phi_i^2 \phi_j^2$$

Where, $\chi_{i,j}$ describes interaction strength between DC proteins, the cytoplasm, and the centrosome. We modeled centrosomal nucleation as a region in the simulation with increased interaction strength as has been done previously to describe nucleation sites[69]. To determine the size of this nucleation region we measured the relative volume of centrosomally-localized DC kinases and β-cat (**Supp. Fig. 3B**). and R_i is the added reaction term with such that

$$R_i(k_{i,j}, \phi_i, \phi_j) = k_{i,j} \phi_i \phi_j \text{ for the creation of } \phi_i$$

and

$$R_i(k_{i,j}, \phi_i, \phi_j) = -k_{i,j} \phi_i \phi_j \text{ for the consumption of } \phi_i.$$

The system is time discretized according to established methods[70]. Assuming that the total free energy of the system decreases to a minimum with time, we use the built-in Newtonian solver in the FEniCS environment to approximate the forward evolution of the system in time. To represent the enzyme activities in the DC, we

model only clients, with scaffolds existing implicitly as the interaction parameters

between system components. Representations are:

Component Variable	Component Name	CH Equation
ϕ_1	GSK3β	$$\frac{\partial \phi_1}{\partial t} = M_1 \nabla^2 \mu_1$$
ϕ_2	CK1α	$$\frac{\partial \phi_2}{\partial t} = M_2 \nabla^2 \mu_2$$
ϕ_3	β-Catenin	$$\frac{\partial \phi_3}{\partial t} = M_3 \nabla^2 \mu_3 - \left(k_{2,3} \cdot \phi_2 \cdot \phi_3 \right)$$
ϕ_4	Phospho-S45 β-Catenin	$$\frac{\partial \phi_4}{\partial t} = M_4 \nabla^2 \mu_4 + (k_{2,3} \cdot \phi_2 \cdot \phi_3) - (k_{1,4} \cdot \phi_1 \cdot \phi_4)$$
ϕ_5	Phospho-S33/S37/S45/T41 β-Catenin	$$\frac{\partial \phi_5}{\partial t} = M_5 \nabla^2 \mu_5 + (k_{1,4} \cdot \phi_1 \cdot \phi_4)$$

ϕ_6	Cytoplasm	$\dfrac{\partial \phi_6}{\partial t} = M_6 \nabla^2 \mu_6$
ϕ_7	Nucleator	$\dfrac{\partial \phi_7}{\partial t} = M_7 \nabla^2 \mu_7$

Table 2.2: Representations of interaction parameters between indicated model system components.

Interaction Parameter

One of the key factors that tunes system behavior is the interaction parameter χ . Assuming a system with constant temperature and pressure, the interaction parameter determines the free energy of the system. When χ is positive between two components, the system will tend to de-mix. If χ is negative between two components they will tend to mix. Lastly, if χ is neutral, the two components are interaction-less. For simplicity, we limited interactions to one of three types: binding (χ ~ -0.1), neutral (χ ~ 0), and separating (χ ~ 2). As noted above we represent the binding action of DC scaffolds implicitly. Scaffold interactions are taken to be of similar strength and were obtained from literature values described in the table below:

Interaction	Behavior	Source

scaffold to GSK3β	Binding	Lee 2003, Pronobis 2017
scaffold to CK1α	Binding	Lee 2003, Pronobis 2017
scaffold to β-cat	Binding	Lee 2003,
scaffold to P1 β-cat	Binding	Schaefer 2019
scaffold to P4 β-cat	Neutral	Lee 2003, Schaefer 2019
scaffold to cytoplasm	Separating	This study
scaffold to centrosome	Binding	This study, Fumoto 2009

Table 3: Binding actions of modeled DC components, provided with citations from which they were obtained.

Given that the APC/Axin interacts with the DC proteins, the following interaction constants were selected for the system with implicit Axin. We set mixing = 2.0, neutral = 0.0, and de-mixing = -0.1.

Simulation Flow

First all parameters are defined (χ, λ, dt, and M). We generate a grid mesh with a closed boundary conditions to mimic the closed system within a cell. A layer is generated for each simulated component and +-5% noise of the initial value is added to induce inhomogeneities. The FEniCS package partial differential solver is called to generate the chemical potential with respect to each component. The final step is to define the output file path and then use the built-in newton solver to generate the simulation. The simulations are then rendered using Paraview software. A detailed

python notebook of the simulations is available on

https://github.com/MZWLab/Lach2022.

Nucleation efficiency parameter scans

We defined the nucleation efficiency of β-cat processing for a given simulation by comparing the ratio of the integrated P4-β-cat to β-cat between identical simulations with and without a nucleator (Supp Fig 3F). This gave us to test the sensitivity of a single metric to alterations in our model's parameters. In Figure 3E we independently altered the simulated phosphorylation rates of CK1 and GSK3, K1 and K2 respectively, to examine how nucleation efficiency was changed. Our findings are intuitive, in that the faster K1 and K2 are, the less nucleation leads to an efficiency gain for the system. In Figure 3F, we examined nucleation efficiency as a function of the free energy of binding between each of the individual DC clients and the cytoplasm, finding that in general, increasing the free energy penalty of client-cytoplasm mixing, drove greater accumulation of clients at the nucleator (Supp Vid. 6) and also increased the nucleation efficiency.

Supplementary Information
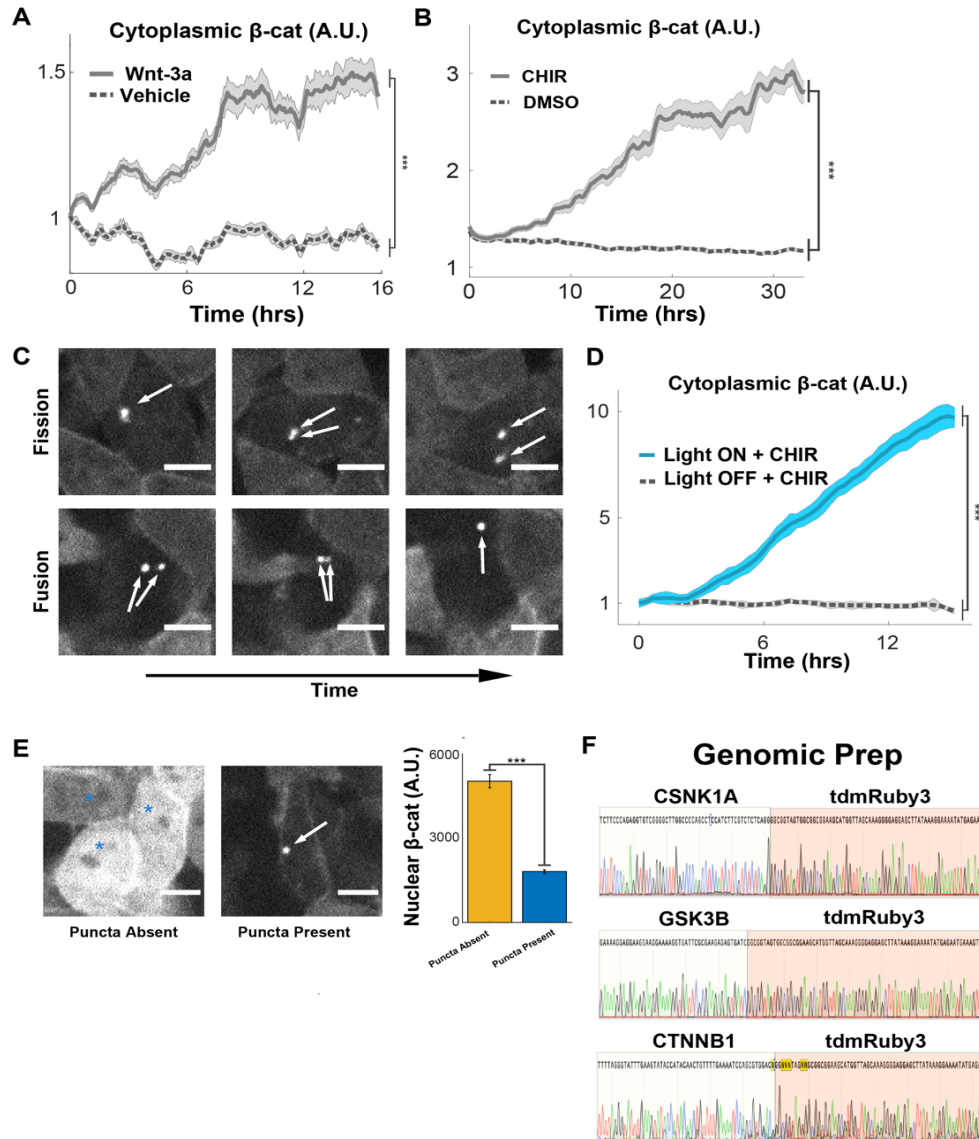
Fig. S2.1. Endogenously expressed β-catenin puncta are inversely correlated with CHIR-mediated Wnt pathway activation and β-catenin accumulation and show hallmarks of dynamic liquidity. A-B. Measurements of CRISPR cytoplasmic tdmRuby3-β-catenin in live 293Ts, data presented as mean fluorescent intensity fraction of t0 +/- s.e.m. (N = 30 cells per condition). C. Montage of single CHIR+ cells containing β-catenin puncta undergoing fission and fusion over time. D. Measurements of CRISPR cytoplasmic tdmRuby3-β-catenin in live 293Ts treated with CHIR, with or without blue light stimulation, data presented as mean fluorescent intensity fraction of t0 +/- s.e.m. (N = 30 cells per condition). E. Left: Representative images of tdmRuby3-β-catenin cells +CHIR for 24hrs. Arrows indicate puncta, asterisks indicate puncta absent. Right: Comparison of mean nuclear β-catenin fluorescence between +CHIR cells with and without visible β-catenin puncta. F. Sanger sequencing traces from genomic PCRs targeting 5' endogenous loci of CRISPR tdmRuby3 knock-ins. Red regions indicate tdmRuby3 insert.
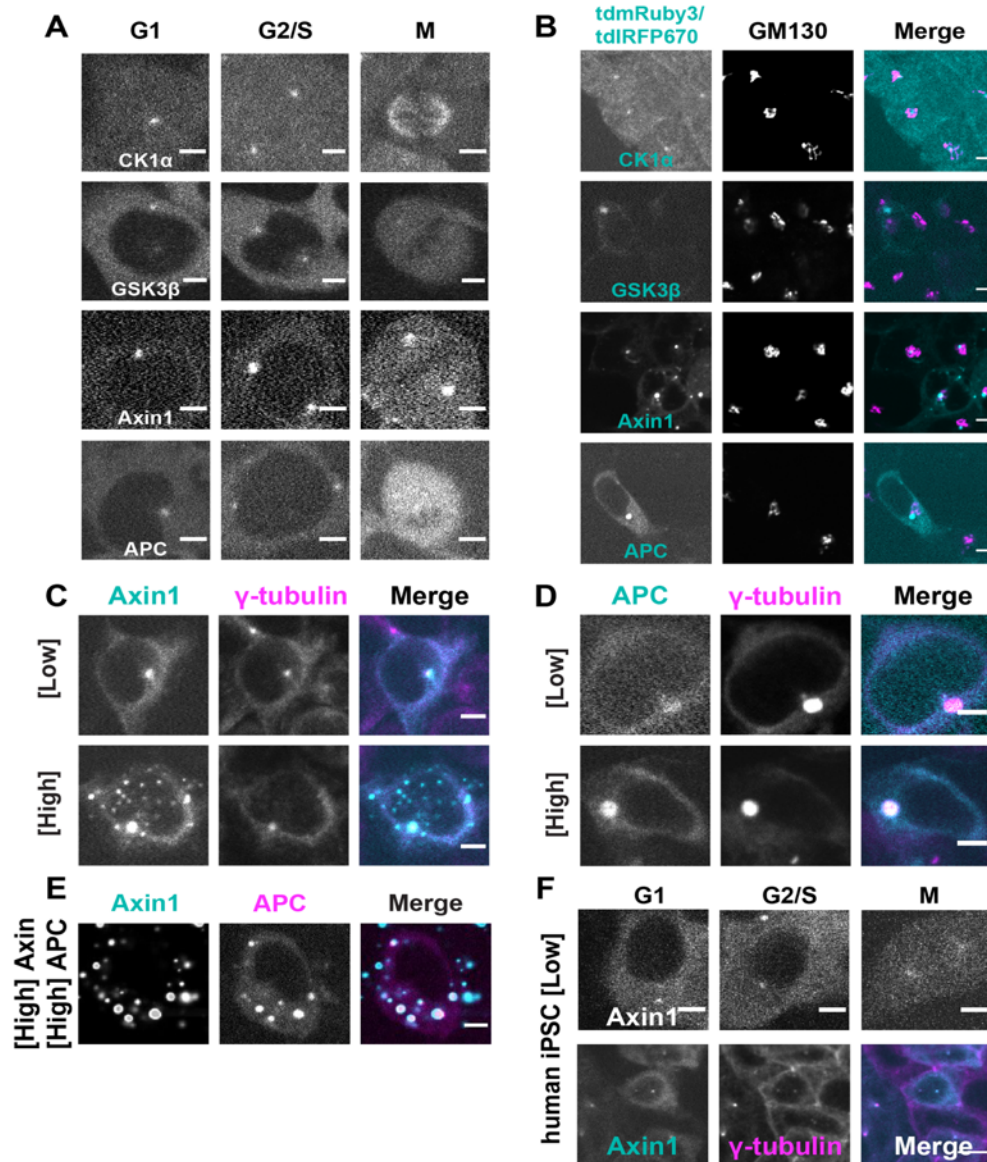
Fig. S2.2. Centrosomal Destruction Complex droplets are spatially correlated with cell cycle progression. A. Representative images of indicated Destruction Complex (DC) components taken live, at various stages of the cell cycle. Montages follow the same cell through time. Scale = 10µm B. Representative fixed images of indicated DC components stained for endogenous GM130. Scale = 10µm. C. Representative images of fixed cells with varying Axin1 induction and co-stained for endogenous γ-tubulin. D. Representative images of fixed cells with varying APC induction and co-stained for endogenous γ-tubulin. E. Representative images of live cells induced to high Axin1 <u>and</u> APC levels simultaneously. F. *Upper:* Representative images of live human induced-pluripotent stem cells (iPSCs) at various stages of the cell cycle. *Lower:* Images of fixed human iPSCs co-stained for endogenous γ-tubulin.

A Mixing parameter ($X_{i,j}$) matrix

Neutral, x = 0 | Mixing, x = -0.1 | De-mixing, x = 2

index j: GSK, CK1, Beta-Catenin, P1 Beta-Catenin, P4 Beta-Catenin, Cytoplasm, Nucleator

index i: GSK, CK1, B-Catenin, P1 Beta-Catenin, P4 Beta-Catenin, Cytoplasm, Nucleator

B lattice

← nucleator

C Centrosomal area

N.S.

% of cytoplasm

β-Cat   CK1α   GSK3β

D comparison of nucleator size

0.005 v/v   0.01 v/v   0.05 v/v

E P4 β-catenin

0.005 v/v
0.01 v/v
0.05 v/v
No nuc. v/v

Volume Fraction — Time Step

F definition of nucleation efficiency

$$E_{nuc} = \dfrac{\left(\dfrac{\int_0^{t_f}\int_\Omega P4BC_{nuc}(t)\,d\Omega dt}{\int_0^{t_f}\int_\Omega BC_{nuc}(t)\,d\Omega dt}\right)}{\left(\dfrac{\int_0^{t_f}\int_\Omega P4BC_{nonuc}(t)\,d\Omega dt}{\int_0^{t_f}\int_\Omega BC_{nonuc}(t)\,d\Omega dt}\right)}$$

integrated P4 β-catenin / integrated β-catenin | nucleated

integrated P4 β-catenin / integrated β-catenin | non-nucleated

G
Intermediate rates

P4 β-cat (% volume) — simulation time

nucleator
$k_1 = k_2 = 8$
$k_1 = k_2 = 32$
$k_1 = k_2 = 128$
no nucleator
$k_1 = k_2 = 8$
$k_1 = k_2 = 32$
$k_1 = k_2 = 128$

High rates

P4 β-cat (% volume) — simulation time

nucleator
$k_1 = k_2 = 512$
$k_1 = k_2 = 1024$
$k_1 = k_2 = 2056$
no nucleator
$k_1 = k_2 = 512$
$k_1 = k_2 = 1024$
$k_1 = k_2 = 2056$

H Efficiency of nucleation

reaction rates k_1 & k_2 — X of all clients to cytoplasm

I DC client to cytoplasm interaction parameter scan

β-catenin | CK1 | GSK

P4 β-cat (% volume) — simulation time

interaction strength X: 2.40, 1.60, 0.80, 0.00

Fig. S2.3. Exploring In Silico Model of Centrosome driven Phase Separation. A. Interaction matrix of each component in the model. Gray indicates a neutral state, blue represents de-mixing, and green represents mixing B. Example lattice used to model the system with example nucleator region in black. After initial conditions are assigned, a model of diffusion operates on grid positions based on modified Cahn Hilliard equations. C. Quantification of the area of centrosomal droplets in comparison of total cell volume taken from CRISPR-tagged cells. Mean is represented by red line. D. Demonstration of the effects of nucleator size on system nucleation process. With a smaller centrosome, the droplet is more densely packed with enzymes whereas a larger centrosome results in droplet separation. E. Quantification of the effect of centrosome size on P4 β-catenin generation. F. Definition of nucleation efficiency as the ratio of the quotient of P4 β -catenin and β-catenin in a nucleated versus an unnucleated system. G. P4 β-catenin accumulation in log2 scan of kinase reaction rates. H. Nucleation efficiency of as a function of reaction rates and X (interaction parameter) of all clients and the cytoplasm. I. Quantification of in silico models of "opto"-β-catenin, "opto"-CK1, and "opto"-GSK. The graphs show increased gain from "opto"-GSK driven separation.
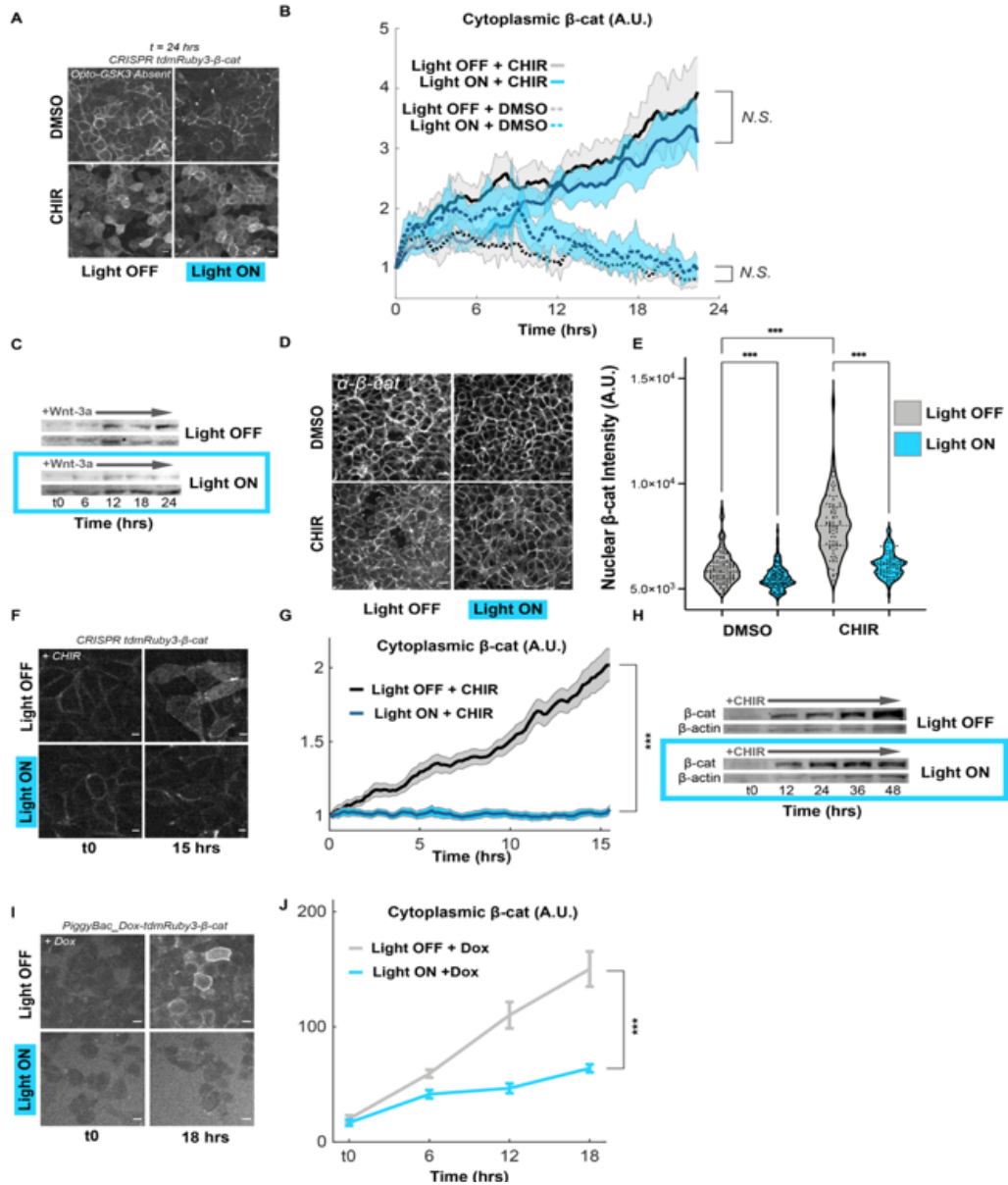
Fig. S2.4. Opto-GSK3 suppresses β-catenin accumulation due to GSK3β inhibition or exogenous chemical induction. A. Representative images of live cells treated with CHIR or DMSO vehicle, with or without blue light stimulation. Scale = 10µm. B. Measurements of experiment shown in A. Data presented as mean +/- s.e.m. (N=30 cells per condition). C. Representative Western blots of lysates from 293Ts bearing Opto-GSK3 and treated with Wnt-3a, with or without blue light stimulation for the indicated time course. D. Representative images of cells bearing Opto-GSK3 fixed and stained for endogenous β-catenin after culture in the indicated conditions for 48 hrs. E. Violin plots of cells from D. F. Representative images of 293Ts bearing Opto-GSK3 and endogenously-expressed tdmRuby3-β-catenin treated with CHIR, with or without blue light stimulation for 24hrs. G. Measurements from experiment shown in F., lines represent fold-change from t0 means +/- s.e.m. for cells in each condition (Light ON N=67, Light OFF N=50 cells). H. Representative Western blots of lysates from 293Ts bearing Opto-GSK3 and treated with CHIR, with or without blue light stimulation for the indicated time course. I. Representative images of 293Ts bearing Opto-GSK3 and Dox-inducible -β-catenin-tdmRuby3 treated with Dox, with or without blue light stimulation. Scale = 10µm. J. Quantification of experiment in I: lines represent absolute means +/- s.e.m for cells in each condition (Light ON N=28, Light OFF N=27 cells).

55

Video S1. Cells with β-cat Puncta Resist β-cat Accumulation in response to CHIR. *Left:* Imaging fields of live tdmRuby3-β-cat cells treated with DMSO control. *Right:* Imaging fields of tdmRuby3-β-cat cells treated with CHIR. Arrows indicate β-cat puncta.

Video S2. Activation of Cry-2-Lrp6c Induces β-cat Accumulation *Left*: Imaging fields of live, unstimulated tdmRuby3-β-cat, Cry2-Lrp6c cells. *Right:* Imaging fields of tdmRuby3-β-cat, Cry2-Lrp6c cells stimulated with blue light throughout indicated timecourse. Videos were taken from cells in the same well.

Video S3. Activation of Cry-2-Lrp6c Results in Dissolution of β-cat Puncta Zoomed videos of cells presented in **Supp. Vid. 2.** Arrows indicate β-cat puncta.

Video S4. In-silico behavior of destruction components with a centrosomal region. In-silico model of phase separation behavior for every component involved in a hypothetical WNT pathway over 100 simulation time steps in the presence of a centrosome.

Video S5. In silico behavior of destruction components without a centrosomal region. In-silico model of phase separation behavior for every component involved in a hypothetical WNT pathway over 100 simulation time steps without the presence of a centrosome.

Video S6. Impact of interaction parameter χ on destruction complex component behavior. In-silico model of the destruction components (CK1α, GSK3β, and β-catenin) at various interaction parameter values (χ) over 100 simulation time steps showing that increasing χ increases separation propensity.

Video S7. Activation of Opto-GSK3 Increases Centrosomal Condensate Partitioning. Zoomed video of Opto-GSK3 cells stimulated with blue light throughout indicated timecourse.

Chapter 3

Cell cycle mediated off-time sensing explains Wnt signaling heterogeneity

Abstract

The Wnt signaling pathway directs proliferation and differentiation of stem cell populations to construct and maintain various tissues in metazoans. Different cell fate outcomes are achieved via selective secretion of Wnt ligands whose identity and concentration act as morphogenic signals for cells poised to respond to these cues. Recent work suggests that Wnt secretion patterns—independent of absolute concentration—likely encode morphogenic information as well, but how dynamics are transduced into cell fate outcomes was previously unknown. Using optogenetics and long-term, live, single-cell imaging of Wnt pathway activation and the cell cycle, we find that the Wnt pathway utilizes off-time sensing to activate transcription and differentiation according to different input frequencies. Additionally, we demonstrate that transcriptional responsivity is predicted by cell cycle phase at signal input cessation, a compelling explanation for the high level of Wnt response heterogeneity observed unsynchronized populations. These findings highlight off-time sensing as an important morphogenic capability of the Wnt pathway and uncover another mode in which Wnt signaling and the cell cycle are connected.

Introduction

Individual cells act both autonomously and cooperatively to form higher-order tissues that execute specialized functions for the organism. To fulfill their role in the tissue, cells process high-dimensional informational landscapes into the relatively simple decisions to proliferate, terminally differentiate and undergo apoptosis; the balance between these decisions determines the tissue's functional capacity[71], repair capacity[72], metabolic demand[73] and disease risk[74]. These decisions are especially important in high-growth or high-turnover tissues—such as the developing embryo[75] and intestine[76]— with large populations of stem cells constantly making fate decisions. A working knowledge of the mechanisms by which ensembles of individual stem cells communicate and coordinate cell fate decisions is fundamental to addressing pathologies related to tissue development and regeneration.

Stem cell fate decisions are largely coordinated by morphogens—secreted protein factors whose temporal, concentration and combinatorial dynamics push cells towards specific identities[77]. The canonical Wnt pathway is a powerful morphogenic system essential for embryogenesis and homeostatic maintenance of differentiated tissues[7]. Wnt signaling directs proliferation and differentiation of various stem cell niches via spatiotemporal secretion and context-specific responses to Wnt ligands[79]. Wnt ligands bind Frizzled/LRP5/6 coreceptors and inactivate the β-catenin (β-cat) destruction complex (DC), causing accumulation and nuclear translocation of β-cat and transcriptional activation of Wnt-target genes[80].

Until recently the Wnt signaling cascade was considered universal and monotonic; i.e. Wnt responsivity is proportional to local ligand concentration and cell type-specific responses are controlled by preexisting differences in the relative expression of pathway components[19]. However, recent work examining the contribution of Wnt dynamics to cell fate outcomes[50,80] has sparked interest in the idea that the pathway is capable of sensing and acting on a rich landscape of signal input patterns independent of ligand concentration. Cells receive endogenous pulsatile[81] and gradient[82] patterns of Wnt in a variety tissues, which are hypothesized to buffer against spurious activation via kinetic proofreading[50,83]. Work in this field has uncovered the relationship between Wnt secretion patterns and cell fate in a variety of tissues, but how these patterns are transduced into morphogenic decisions remained unclear.

Using optogenetics, live-cell reporters of Wnt activation and the cell cycle and single-cell tracking, we show that the Wnt pathway computes input signal duration and cell cycle phase into transcriptional activation upon removal of activating stimulus. We find evidence that the shift between Wnt ON and Wnt OFF states can be thought of as a switch between 'reading' and 'writing' modes—in which transcriptional response is delayed until the activity pulse is fully recorded. Finally, we demonstrate that the Wnt reading/writing module is sensitized to detection of short (> 1hr) and long (8-16hr) pulses of activation compared to intermediate (2-6hr) pulses. These findings suggest that the Wnt pathway integrates cell cycle phase and activity pulse frequency to coordinate distinct morphogenic responses from individual cells within a tissue.
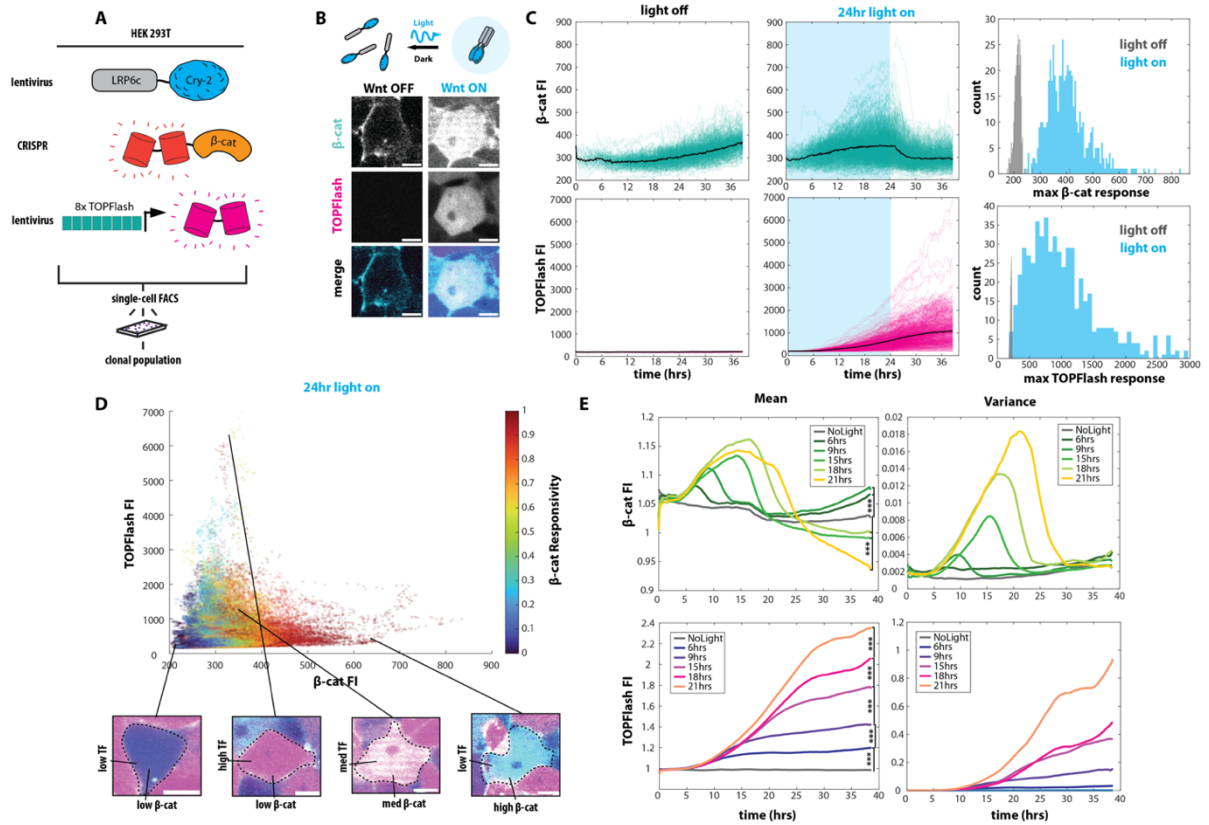
Figure 3.1: Wnt responsivity heterogeneity in clonal 293T population. (A) Schematic of Wnt I/O cells containing lentiviral optogenetic LRP6c, CRISPR tdmRuby3-β-cat, lentiviral 8X-TOPFlash-tdIRFP, clonally FACS-sorted. (B) Representative examples of tdmRuby3-β-cat and tdIRFP accumulating in response to 24hrs of blue light activation in Wnt I/O cells. (C) *Left and center columns:* Single-cell mean fluorescent intensity (MFI) traces (N = 321-567 cells, 4 biological replicates per condition) of tdmRuby3-β-cat and (TOPFlash) tdiRFP measurements from live Wnt I/O cells tracked during exposure to activating blue light or no light controls. Blue background indicates light on, white indicates light off. *Right column:* Histograms of maximum MFI for each track across timecourse. (D) *Center:* Scatter plot of cells measured during 24 hrs of blue light activation; points colored by min-max normalized β-cat MFI responsivity. *Outer:* Representative examples cells from each quadrant of scatter plot. (E) *Left Column:* Means of means of live, single-cell β-cat and TOPFlash MFI traces from indicated conditions (N = 321-595 cells, 4 biological replicates per condition, see Supplementary information for significance values). *Right Column:* Variance of *left column* populations.

Results

Cells respond heterogeneously to identical Wnt pathway inputs

To determine the relationship between Wnt pathway activation, β-cat concentration and Wnt target gene transcription dynamics we constructed a 293T Wnt input/output cell line bearing transposon integrated optogenetic LRP6c (oLRP6), CRISPR-tagged tdmRuby3-β-cat and lentivirally integrated 8X-TOPFlash-tdIRFP, allowing for arbitrary control of pathway activation and visualization of β-cat concentration and integrated transcriptional 'history' of single cells in real-time ('Wnt I/O', **Fig. 3.1A**). To control for heterogenous expression of oLRP6 and TOPFlash, clonal populations were generated via single-cell fluorescence-activated cell sorting (FACS) and a highly responsive clone selected for subsequent experimentation (**Fig. 3.1A-B**).

Wnt I/O cells were activated, imaged and tracked continuously for 24hrs via 455nm light stimulation followed by a 14hr relaxation period to see how β-cat levels and Wnt-target gene transcription respond to prolonged pathway activation and subsequent return to baseline. See **Fig. 3.1C**: Surprisingly, individual cells display highly heterogenous responses to this identical oLRP6 activation pattern at both β-cat and TOPFlash pathway nodes. We reasoned that a hidden variable controlling pathway responsivity in individual cells is responsible for the observed heterogeneity and sought to determine whether β-cat responsivity and TOPFlash responsivity are correlated in single cells. See **Fig. 3.1D**: β-cat accumulation across the timecourse is a poor indicator of TOPFlash accumulation and cells containing high levels of β-cat almost always showed weak TOPFlash signal, suggesting an inverse relationship between β-cat responsivity and transcriptional activation in time. We thought that this

61

effect may be due to negative feedback exerted on the pathway in response to prolonged activation and so next asked whether a similar pattern is observed in populations activated for less than 24hrs. See **Fig. 3.1E**: Similar to those in the 24hr light ON condition, Wnt I/O cells exposed to 6,9,15,18, and 21 hrs of oLRP6 activation displayed heterogeneous β-cat and TOPFlash responses; despite this, activation time was highly predictive of population means. Interestingly, β-cat concentration variance depended on activation time, with peak variance observed just after cessation of oLRP6 activation, while TOPFlash variance increased continuously throughout the timecourse.

Cell cycle phase predicts responsivity of Wnt-target transcription to pathway activation

Our previous work[85] as well as others[86,87] have shown that Wnt pathway components essential for regulating β-cat stability undergo biophysical and chemical changes in response to cell cycle progression. We thus hypothesized that cell cycle stage may be a source of Wnt responsivity heterogeneity in our system. To map Wnt responsivity to cell cycle progression, a modified version of the fluorescence ubiquitination cell cycle indicator (FUCCI[88]) in which RFP was swapped for mTagBFP2 ('Bluecci') to allow for simultaneous monitoring of the cell cycle, β-cat and TOPFlash accumulation, was lentivirally integrated into our Wnt I/O 293T line, and a clonal population was obtained as above (**Fig. 3.2A**). To determine the relationship between cell cycle phase and Wnt pathway responsivity, cells were activated, imaged and tracked across a 24hr activation period. Relative expression
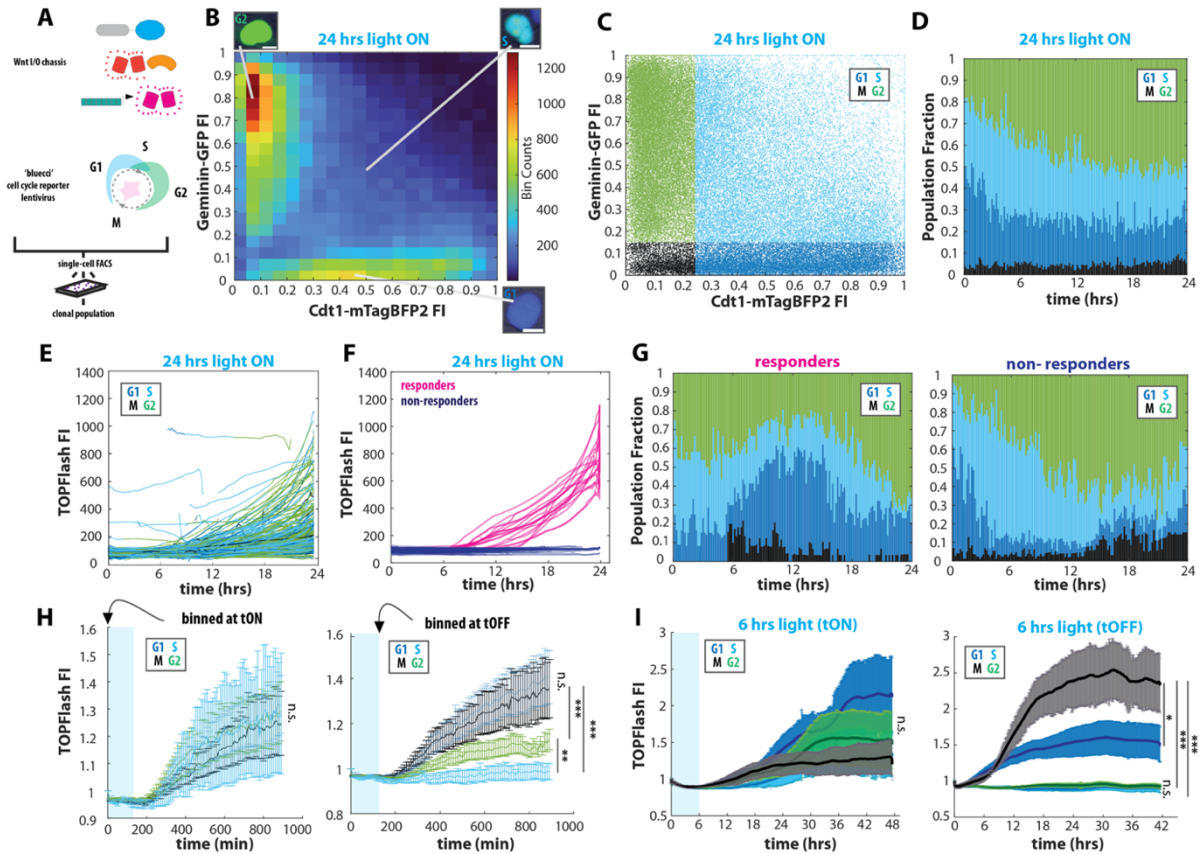
Figure 3.2: Cell cycle phase at cessation of Wnt signal predicts transcriptional activation trajectory. (A) Schematic of Wnt I/O cells containing lentiviral optogenetic LRP6c, CRISPR tdmRuby3-β-cat, lentiviral 8X-TOPFlash-tdIRFP, lentiviral Cdt1-mTagBFP2, lentiviral Geminin-GFP, clonally FACS-sorted. (B) Heatmap displaying min-max normalized mean fluorescent intensity (MFI) of Cdt1-mTagBFP and Geminin-GFP in cells stimulated with blue light for 24hrs (N = 100168 cell observations from 617 tracks across 4 biological replicates). 'Hot' regions were used to define cutoff regions for classification into cell cycle stages in panel (C) Demonstration of cutoff criteria for classification of cells into cell cycle phases. (D) Stacked bar plots displaying the fraction of total cells classified into each cell cycle phase (Mean of 139 cell observations per timepoint). (E) Single-cell TOPFlash traces colored by cell cycle classification at each measurement points during 24hrs of blue-light stimulation. (F) Single-cell traces of 'responders' (top 10% fold-change over track timecourse) and 'non-responders' (bottom 10% fold-change over track timecourse) from population in E. (G) Stacked bar plots displaying the fraction of total cells classified into each cell cycle phase for 'responders' and 'non-responders' in F (Mean of 56 cell observations per timepoint). (H) Normalized mean +/- SEM for cells classified in each stage of the cell cycle at start of 2hr light stimulation ('tON', left panel) or end of stimulation ('tOFF', right panel). N = 60 cells. (I) Normalized mean +/- SEM for cells classified in each stage of the cell cycle at tOFF after 6hr (left panel), 12hr (middle panel), 24hr (right panel) of light stimulation (N = 50 – 61 cells per condition).

of Cdt1-mTagBFP2 and Geminin-GFP was measured and used to classify single

cells as being in G1, S, G2, or M phases (Fig. 2B-C). In-line with what has been

reported by others[84], prolonged Wnt pathway activation led to rearrangement of cell

63

cycle representation in the population: a steady increase in the G2 fraction accompanied by a concomitant decrease in G1 fraction as the timecourse progressed (**Fig. 3.2D**). Along with this, single-cell β-cat and TOPFlash dynamics displayed heterogenous responses to 24hrs of activation (**Fig. 3.2E**). Because the timescales over which the Wnt pathway and cell cycle interact were unknown (i.e. does the cell cycle control response to activation duration, start time or end time?), we decided to compare cell cycle distributions of populations of highly transcriptionally responsive (80th percentile and above) cells with weakly responsive (20th percentile and below) cells (**Fig. 3.2F**). See **Fig. 3.2G**: High transcriptional responders in the set showed cell cycle distributions biased toward G1 and M compared to low responders which displayed higher fractions of cells in S and G2. Intriguingly, the largest differences between population distributions appeared in hours 6-18 of pathway activation, the same range over which all high responders first activated transcription. We also noticed that, over the 24hr activation period, even the earliest responding cells did not show transcriptional activation until approximately 6-8hrs of oLRP6 stimulation.

This led us to hypothesize that rather than continuously propagating receptor-level activation into transcriptional activation, the Wnt pathway contains a 6-8hr 'reading' period in which cells integrate signal input and cell cycle phase before 'writing' the output of target gene transcription. To test this, we tracked cells activated for 2hrs followed by a 12hr rest period to determine whether: 1) transcriptional activation would begin earlier than 6-8hrs observed in the 24hr continuous activation condition, and 2) cell cycle phases still predicts transcriptional

response at shorter activation timescales. See **Fig. 3.2H**: 2hr activation followed by rest resulted in TOPFlash accumulation beginning at approximately 3hrs, supporting the 'reading'/'writing' hypothesis. We next wondered whether the Wnt pathway incorporates cell cycle phase into transcriptional activation at the start (tON) or end (tOFF) of signal input. Strikingly, there was high heterogeneity and no significant difference between transcriptional activation of cells in G1, S, G2 or M phases at tON of the 2hr Wnt input pulse, but categorization by cell cycle phase at tOFF resulted in diversion between groups and a marked reduction in in-group heterogeneity. Notably, cells in G1 and M phases at tOFF showed stronger transcriptional activation than cells in G2, which were in-turn more responsive than cells in S. Further, to determine if tOFF cell cycle phase is predictive of transcriptional response at longer activation timescales we tracked cells in each stage of the cell cycle stimulated for 6hrs (**Fig. 3.2I**). A similar trend was observed in the 6hr light ON conditions, with cells in G1 and M at tOFF showing stronger transcriptional responses than those in S or G2. Again, categorization at tOFF showed reduced in-group heterogeneity compared to categorization at tON.

Wnt off-time sensing controls downstream pathway activation and stem cell fate
In light of the finding that the Wnt pathway incorporates tOFF into transcriptional activation, we returned to our initial Wnt I/O line to explore the effects of different durations and patterns of Wnt stimulation on transcriptional output. First, we sought to define the temporal bounds of the 'reading' phase by stimulating with pulses of light for different durations followed by rest. See **Fig. 3.3A**: Transcriptional activation

65
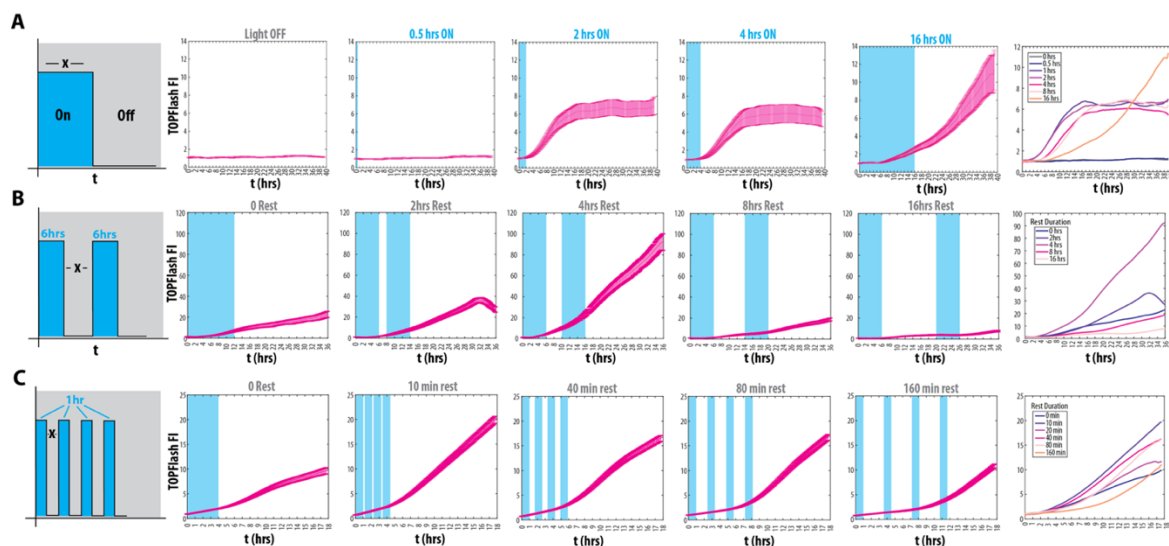
Figure 3.3: Dynamical Wnt inputs reveal off-time sensing. (A-C) *Left-most panels*: Schematic depictions of light stimuli pertaining to each row; blue bars indicate light ON periods, grey spaces indicate light OFF periods, 'x's refer to independent variable in each row. (A) Normalized mean +/- SEM TOPFlash values for cell populations stimulated with a single pulse for the indicated durations; right-most panel shows overlaid means of first 7 panels for comparison (N = 20 cells per condition, across 3 biological replicates). (B) Normalized mean +/- SEM TOPFlash values for cell populations stimulated with two, 6hr pulses separated by the indicated durations of rest in between; right-most panel shows overlaid means of first 5 panels for comparison (N = 54 - 247 cells per condition, across 4 biological replicates). (C) Normalized mean +/- SEM TOPFlash values for cell populations stimulated with 4, 1hr pulses separated by the indicated durations of rest in between; right-most panel shows overlaid means of first 6 panels for comparison (N = 441 - 570 cells per condition, across 4 biological replicates).

was observed following a minimum of 1hr stimulation and increasing stimulation time resulted in time-shifted sigmoidal curves of stereotyped TOPFlash accumulation through 8hrs of input. By contrast, 16hrs stimulation resulted in more gradually building, but higher max transcriptional activation, suggesting distinct response profiles between short-term and long-term inputs and confirming that the max reading window is approximately 6 hrs before transcriptional activation occurs without signal cessation.

Implicit in the reading/writing hypothesis is the feature that the Wnt pathway stores input signal duration which is then read-out at the end of a signal pulse. Based on this idea, we sought to test how Wnt pathway responsivity is affected by

66
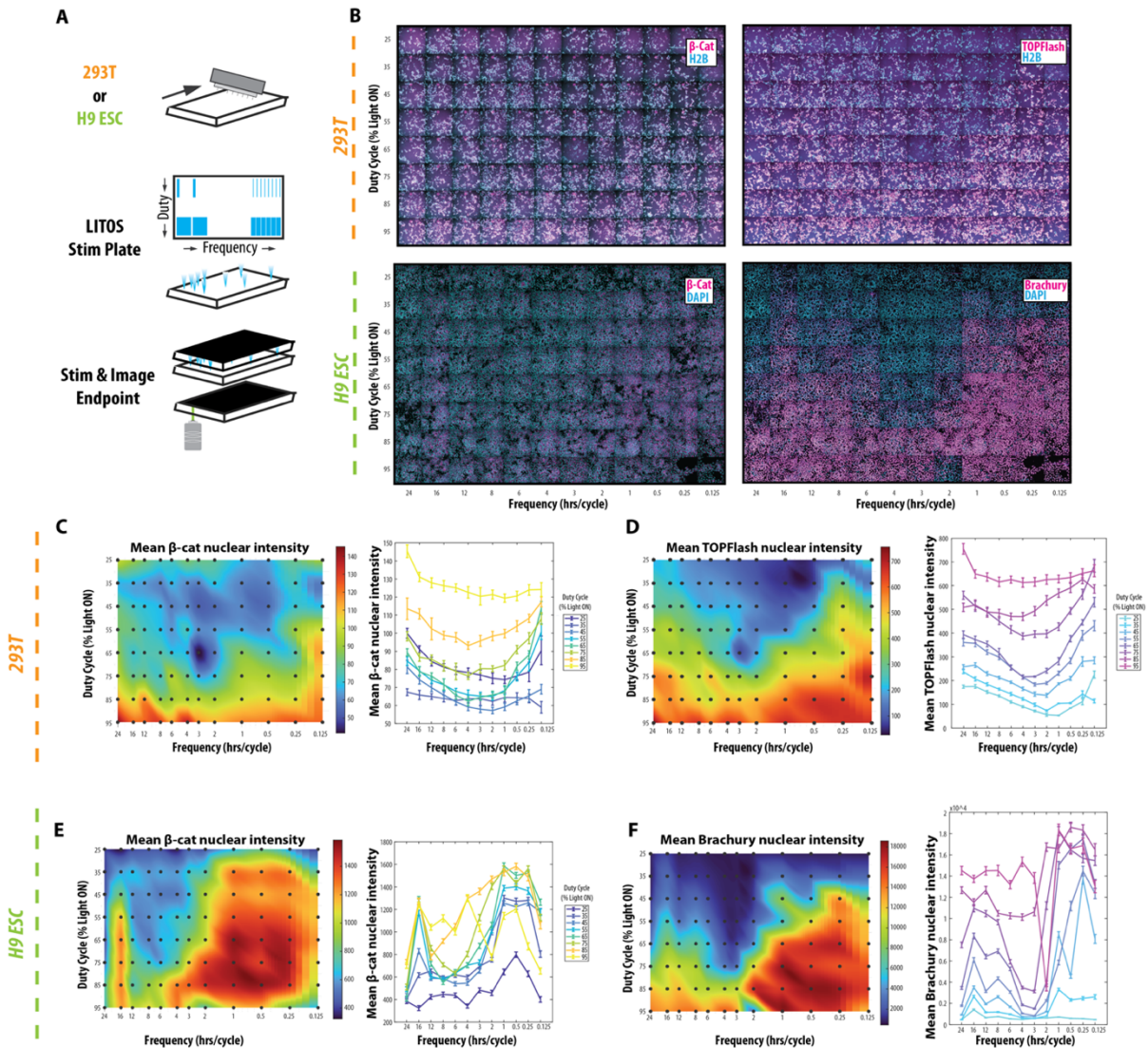
memory of previous activation. See **Fig. 3.3B**: Wnt I/O cells were exposed to two 6hr

pulses of light separated by a variable rest period. Surprisingly, populations that

experienced a short (below 4hrs) rest period between 6hr pulses showed higher

transcriptional activation than those activated continuously for 12hrs. This effect was

diminished in 8 and 16hr rest conditions, potentially due to insufficient time for signal

to accumulate following the 2nd pulse or negative feedback. The finding that a period

of rest between pulses of Wnt activity alters transcriptional response to the same

total duration of input led us to ask whether a similar pattern of off-time sensing

Figure 3.4: Dynamical inputs reveal frequency-responsive transcriptional and cell fate landscapes. (A) Schematic of 96-well optogenetic stimulation plate workflow. (B) Example images from each well of indicated cell types. Note: 293Ts received indicated stimulation conditions for 48hrs before fixation and imaging; H9s received the same stimulation conditions for 24hrs before fixation and imaging. (C) *Left:* Heatmap displaying mean nuclear intensity of tdmRuby3-β-cat in 293Ts stimulated with the indicated duty cycle and frequency of stimulation pulses for 48hrs (N = 81 – 590 cells per condition across 4 biological replicates). *Right:* Mean +/- SEM values for cells in each row (holding duty cycle constant within each line) from *left.* (D) *Left:* Heatmap displaying mean nuclear intensity of TOPFlash_iRFP in cells stimulated with the indicated duty cycle and frequency of stimulation pulses (N = 81 – 590 cells per condition). *Right:* Mean +/- SEM values for cells in each row (holding duty cycle constant within each line) from *left.* (E) *Left:* Heatmap displaying mean nuclear intensity of tdmRuby3-β-cat in h9 ESCs stimulated with the indicated duty cycle and frequency of stimulation pulses for 24hrs (N = 144 – 529 cells per condition across 4 biological replicates). *Right:* Mean +/- SEM values for cells in each row (holding duty cycle constant within each line) from *left.* (F) *Left:* Heatmap displaying mean nuclear intensity of α-Brachury in h9 ESCs stimulated with the indicated duty cycle and frequency of stimulation pulses for 24hrs (N = 144 – 529 cells per condition across 4 biological replicates). *Right:* Mean +/- SEM values for cells in each row (holding duty cycle constant within each line) from *left.*

persists over the course of multiple, short activation pulses. See **Fig. 3.3C**: In-line with the trend observed in the 2-pulse series, 4, 1hr pulses of activation interspersed with shorter periods of rest increased transcriptional response compared to cells in the no-rest condition, but longer periods of rest led to decreased transcriptional response.

Together, these results suggest that individual pulse duration and individual rest duration interact to produce differential Wnt responses to the same total integrated stimulus. Cells receiving Wnt input in the body are subject to pulsatile dynamics[89] that are thought to direct cell fate decisions, but the logic of these patterns remained to be explored thoroughly. To map a wide range of possible pulse/rest durations and integrated activation time inputs to Wnt pathway activation outputs, a light stimulation device capable of arbitrarily activating individual wells of a tissue culture plate[90] was used to co-vary integrated activation duration (duty cycle) and pulse duration (frequency) over an extended timecourse (**Fig. 3.4A**). First, we probed the effects of stimulation duty cycle and frequency on β-cat concentration

and transcriptional activation in 293Ts over 48hrs. Response landscapes of both β-cat and TOPFlash displayed similar trends: holding frequency constant, higher duty cycle resulted in increased pathway response, while holding duty cycle constant, frequency showed a biomodal trend with maxima generally at high and low frequencies (**Fig. 3.4B** *top,* **Fig. 3.4C-D**). Notably, the effect of frequency was greatest at low to intermediate levels of activation, suggesting that very high stimulation duty cycle overcomes the effect of frequency.

Finally, to determine whether the observed trends in 293Ts give rise to differences in Wnt-driven cell fate decisions, a pseudo-clonal H9 human embryonic stem cell (hESC) line bearing oLRP6 and CRISPR tdmRuby3-β-cat was generated, exposed to the same landscape of activation conditions, fixed and stained for markers of pluripotency and mesoderm lineage commitment. See **Fig. 3.4B** *bottom,* **Fig. 3.4E-F**: Strikingly, similar effects of duty cycle and frequency were observed both at the levels of β-cat and Brachury expression, again with local maxima at frequencies of 15mins and 16hrs.

Discussion

In an effort to construct a systems-level relationship between Wnt input, β-cat accumulation and transcriptional activation of Wnt-target genes, we find that the Wnt pathway integrates temporal input and cell cycle phase into transcriptional activation and cell fate decisions. Long-term single cell-tracking of Wnt activation history and cell cycle progression in single cells revealed heterogeneous individual responses to Wnt stimulation; population means have a linear relationship to simple signal inputs,

69

but fail to capture individual activation dynamics. Our findings suggest that Wnt responsivity is strongly influenced by the cell cycle phase in which Wnt input is removed.

Our results reveal a novel property of the canonical Wnt pathway: transcriptional triggering by 'off-time' sensing. We observed that Wnt stimuli pulses of durations less than 1 hr result in no measurable transcription, those between 1hr and 8hrs give a time-shifted singular ('short term') response and those greater than 8 hrs result in a more gradual, but higher amplitude response. These findings indicate that the Wnt pathway is sensitive to input durations and has the ability to couple the timing of downstream output to cessation of upstream input. Unlike linear signaling cascades like the MAPK/ERK pathway in which the time between receptor activation and transcription is coupled to the level of transcriptional output[91], the Wnt pathway appears to have the ability to control timing and magnitude independently. Wnt off-time sensing likely contributes to the effect of receptor activation frequency on transcriptional output and cell fate. Further work is needed to determine whether such 'resonant' frequencies are found in endogenous niches of Wnt secretion— indicating that the Wnt pathway evolved to respond to certain signal patterns—or are merely an exploitable design characteristic. Dynamic sensitivities may provide a novel avenue for treating aberrant Wnt activation in disease states.

How does Wnt off-time sensing work, and why is it limited to 8 hrs of receptor activation? A mechanism predicted to have such behavior is a biophysical 'sink' at the LRP6 signalosome; upon receptor activation an unknown factor accumulates or acquires post-translational modifications at the signalosome and is released to co-

activate transcription when ligand is no longer present. At longer activation durations the signalosome becomes saturated with the factor and begins to 'leak' modified factor into the cytoplasm, initiating transcription while LRP6 remains active. Such a mechanism aligns with the findings that many DC components are recruited to the signalosome and phosphorylated in response to Wnt ligand binding[56,92]. A promising approach for identifying such factors would be to screen for genes necessary for suppressing Wnt target gene transcription within the 8hr 'listening' window in the presence of activated oLRP6.

This work reinforces the already deep connection between the canonical Wnt pathway and the cell cycle. We found that cell cycle phase at tOFF, but not tON, is strongly predictive of transcriptional response to LRP6 activation. Wnt pathway components interact with cell cycle effectors at multiple locations and signaling nodes in the cell. For example, it is known that the Cyclin-Y/CDK14 complex, whose levels oscillate with the cell cycle and peak at G2/M[87], phosphorylates LRP6 and increases its sensitivity to Wnt[93]. Further, all DC components necessary for β-cat phosphorylation are localized to a liquid condensate nucleated by the centrosome which is subject to biophysical regulation in step with the cell cycle[85]. It was recently shown that β-cat's network of gene targets is highly dynamic and influenced by cell identity and chromatin accessibility[89], suggesting that cell cycle-mediated epigenetic states, tissue-specific expression of transcription factors and mitotic potential may contribute to Wnt responsivity at the level of transcription. Our finding that cell cycle-mediated responsivity appears to be coupled to off-sensing adds another layer of complexity to the interplay between the Wnt pathway and the cell cycle. Future work

targeting this connection may utilize a combination of live-cell tracking and spatiotemporally-targeted optogenetic stimulation to access novel Wnt activation and cell identity states in unsynchronized tissues.

Collectively, our results call attention to the importance of dynamics in cell signaling. A cell's state is constantly in flux, perpetually sensing and responding to intrinsic and extrinsic information about its identity, health, location and function in the tissue. Precise temporal control of signaling inputs coupled with live readouts of cell states and signaling outputs can reveal novel connections and design principles governing the essential cellular processes that give rise to health and disease.

Materials and Methods

Cell Lines. Human 293T cells were cultured at 37°C and 5% CO2 Dulbecco's

Modified Eagle Medium, high glucose GlutaMAX (Thermo Fisher Scientific,

10566016) medium supplemented with 10% fetal bovine serum (Atlas Biologicals, F-

0500-D) and 1% penicillin-streptomycin. Experiments in human Embryonic Stem

Cell (hESC) lines were performed using the H9 hESC cell line purchased from the

William K. Bowes Center for Stem Cell Biology and Engineering at UCSB. Cells

were grown in mTeSR™ Plus medium (Stem Cell Technologies) on Matrigel®

(Corning) coated tissue culture dishes and tested for mycoplasma in 2-month

intervals.

Cloning of Lentiviral Overexpression Constructs. pBOB_EF1_FastBluecci_Puro was

constructed via subcloning human tdmTagBFP2 provided by Ryan Lach into the

pBOB-EF1-FastFUCCI-Puro lentiviral expression vector (obtained from Addgene,

plasmid #86849) bearing an EF1-α promoter and flanking long-terminal repeats

(LTRs) using Gibson Assembly (New England BioLabs Inc., E2611L) according to

supplier instructions. Each of the PCR fragments used were amplified using the

following primers:

pBOB Backbone fwd:

CAGCAAACTCGGCCATAAGCTCAATtacagcatgctgcctagcctcg rev:

TATTTTCCTTGATGAGTTCACTCATggatcccaattcttaattaatcacgacacctg.

tdmTagBFP2 fwd: ATGAGTGAACTCATCAAGGAAAATATGCACATG rev: ATTGAGCTTATGGCCGAGTTTGCTG

All above constructs were transformed into Top10 competent cells prepared using Mix & Go E.coli Transformation Kit and Buffer set (Zymo Research #T3002), cultured on LB agar plates to select for antibiotic resistance using standard workflows for molecular cloning and DNA production(49). Plasmid DNA was purified using the Zyppy Plasmid Miniprep kit (Zymo Research #D0436). In addition to antibiotic selection, constructs were verified via Sanger sequencing using primers targeting fusion junctions of relevant construct domains.

Lentiviral Production and Transduction. Production of lentivirus carrying FastBluecci_Puro was accomplished via co-transfection of pBOB_EF1_FastBluecci_Puro, psPAX2 (obtained from Addgene, plasmid #12260) and pMD 2.G (obtained from Addgene, plasmid #12259) at a 1: 0.8 : 0.45 *mass* ratio using standard PEI-based transfection procedures (CITE,50). Cells were incubated for 24 hours before replacing with fresh media and allowing for lentiviral production for an additional 48 hours. Supernatant was harvested, filtered through 0.45um syringe filter and added to plated cells for transduction.

Wnt I/O 293T Cell Line generation. Clonal 293Ts containing CRISPR tdmRuby3-β-cat and oLRP6_Puro were obtained from Ryan Lach and constructed as described previously(CITE). Cells were co-transfected with pPig_8X-TOPFlash-tdIRFP_Puro obtained from Ryan Lach and Super PiggyBac Transposase (System Biosciences

74

cat#: PB210PA-1) using manufacturers recommendations and standard PEI-based transfection procedures. Cells were incubated for 24hrs before replacing with fresh media. Cells were then subject to 12hrs of continuous 455nm light activation on the LITOS and single-cell FACS sorted for tdmRuby3+, tdIRFP+ into a 96-well plate. Cells were monitored for growth over 14 days, only wells containing single colonies (arising from attachment of a single clone) were kept for subsequent processing. Prospective clonal populations were then imaged pre- and post 12hr light activation to screen for low baseline expression of β-cat and TOPFlash and medium-high expression post activation.

This same process was repeated to generate clonal Wnt I/O 293Ts bearing the Bluecci reporter: Following transduction of clonal Wnt I/O cells with FastBlucci_Puro lentivirus, single-cell FACS was performed to seed tdmRuby3+, tdmTagBFP2+, GFP+ triple-positive clonal populations into a 96-well plate. Cells were monitored for growth over 14 days, only wells containing single colonies were kept for subsequent processing. Prospective clonal populations were then imaged pre- and post 12hr light activation to screen for strong presence of green/blue nuclear signal, low baseline expression of β-cat and TOPFlash and medium-high expression post activation.

Wnt I/O H9 Cell Line generation. Clonal beta-catenin reporter lines were generated through CRISPR/Cas9-mediated homology directed repair using analogous methods to 293T counterparts. Accutase digested single hESCs were seeded onto Matrigel coated 12 well plates and transfected with Lipofectamine™ Stem Transfection

Reagent (Invitrogen, STEM00015) according to manufacturer recommendations.

Once the cells grew to confluency, they were selected with 2µg/mL puromycin in

mTeSR plus. Clonal populations were isolated through single cell sorting with the

SH800 Sony Cell Sorter and expanded. The resulting population was screened and

periodically treated with puromycin to ensure they mimicked canonical Wnt signaling

upon optogenetic stimulation.

Antibodies and Immunofluorescence. Primary antibodies used to stain for Brachury

and Sox2 in H9s were α-Sox2 (Cell Signaling 3579, 1:500 dil.) and α-Brachury (RnD

AF2085, 1:500). Secondary antibodies used were α-Rbt-Alexa-488 (Thermofisher

A21206, 1:1000) and α-Gt-Alexa-647 (Thermofisher A21447, 1:1000). Tissue

fixation and staining was carried out using standard protocols using cold methanol[64].

Immunofluorescent samples were imaged using confocal microscopy (see below).

Nuclear stain was carried out using NucBlue Live ReadyProbes (Hoescht 33342,

R37605) according to manufacturer's instructions.

Imaging. All live and fixed cell imaging experiments were carried out using a Nikon

W2 SoRa spinning-disk confocal microscope equipped with incubation chamber

maintaining cells at 37°C and 5% CO2. Glass-bottom culture plates (Cellvis # P96-

1.5H-N) were pre-treated with bovine fibronectin (Sigma #F1141) in the case of

293Ts or Matrigel in the case of H9s, and cells were allowed to adhere to the plate

before subsequent treatment or imaging.

Optogenetic Stimulation. Spatial patterning of light during timelapse fluorescent imaging sessions was accomplished via purpose-built microscope-mounted LED-coupled digital micromirror devices (DMDs) triggered via Nikon NIS Elements software. Stimulation parameters (brightness levels, duration, pulse frequency) were optimized to minimize phototoxicity while maintaining continuous activation of Cry-2. For DMD-based stimulation on the microscope, the final settings for 'Light ON' were 25% LED power (λ = 455nm), 2s duration pulses every 30s. For experiments that did not require frequent confocal imaging, cells were stimulated via a benchtop LED array purpose-built for light delivery to cells in standard tissue culture plates ('LITOS'[90]). The same light delivery parameters were used for LITOS-based stimulation as for microscope mounted DMDs. Light was patterned to cover the entire surface of intended wells of plates used, rather than a single microscope imaging field.

Image Analysis. All quantification of raw microscopy images was carried out using the same general workflow: background subtraction > classification > measurement > normalization > statistical comparison. When possible, subcellular segmentation of nuclear fluorescence was performed via context-trained deep learning-based Cellpose 2.0 algorithm derived from the 'nuclei' or 'cyto2' pretrained models pre-packed with the current Cellpose software distribution available here: https://github.com/mouseland/cellpose [94]. Single-cell tracking and raw measurements were performed with the 'LAP Tracker' function in the TrackMate plugin for imageJ available here: https://imagej.net/plugins/trackmate/ [95] Tracks

containing fewer than 50 contiguous frames (spurious or exited camera field of view) were omitted from subsequent analysis. When experimental conditions did not permit automated segmentation of nuclear fluorescence, cells were selected at random using custom ImageJ macro that generates random ROIs (available upon request). Unless otherwise noted, mean fluorescent intensity of regions of interest were measured and subsequently processed. Raw measurements were compiled, processed, and plotted via custom Matlab scripts, available upon request.

Statistical Analysis.

p value range	Symbol
$0.01 < p < 0.05$	*
$0.001 < p < 0.01$	**
$p < 0.001$	***

Table 3.1: All statistical tests were carried out on final grouped datapoints presented in figures using independent samples t-tests (Matlab function "ttest2").

Supplementary Information

Figure	Panel	Sample Pop	Reference Pop	p value	symbol
1	E	6hr bcat	No Light bcat	2.91E-09	***
1	E	9hr bcat	No Light bcat	5.61E-15	***
1	E	15hr bcat	No Light bcat	2.37E-07	***
1	E	18hr bcat	No Light bcat	2.32E-03	***
1	E	21hr bcat	No Light bcat	2.54E-43	***
1	E	6 hr TF	No Light TF	8.95E-46	***
1	E	9hr TF	6hr TF	7.68E-12	***
1	E	15hr TF	9hr TF	3.34E-09	***
1	E	18 hr TF	15 hr TF	3.12E-05	***
1	E	21 hr TF	18hr TF	1.75E-05	***
2	Hleft	M	G1	5.80E-01	ns
2	Hleft	M	S	5.50E-01	ns
2	Hleft	M	G2	5.70E-01	ns
2	Hleft	G1	S	4.50E-01	ns
2	Hleft	G1	G2	9.90E-01	ns
2	Hleft	S	G2	3.40E-01	ns
2	Hright	M	G1	5.87E-01	ns
2	Hright	M	G2	7.90E-03	**
2	Hright	M	S	7.70E-04	***
2	Hright	G1	G2	3.16E-03	**
2	Hright	G1	S	7.20E-05	***
2	Hright	S	G2	1.63E-03	**
2	Ileft	M	G1	1.52E-02	*
2	Ileft	M	S	2.91E-09	***
2	Ileft	M	G2	1.14E-11	***
2	Ileft	G1	S	2.29E-04	***
2	Ileft	G1	G2	4.22E-05	***
2	Ileft	S	G2	2.31E-01	ns
2	Iright	G1	S	2.24E-01	ns
2	Iright	G1	G2	3.55E-01	ns
2	Iright	G1	M	1.08E-01	ns
2	Iright	S	G2	7.59E-01	ns
2	Iright	S	M	6.27E-01	ns
2	Iright	G2	M	4.44E-01	ns

Table 3.2: Results of statistical tests performed.

References

1. Hogan, B. L. Morphogenesis. *Cell* **96**, 225–233 (1999).

2. Coudert, Y., Harris, S. & Charrier, B. Design Principles of Branching Morphogenesis in Filamentous Organisms. *Curr. Biol.* **29**, R1149–R1162 (2019).

3. Ho, B., Baryshnikova, A. & Brown, G. W. Unification of Protein Abundance Datasets Yields a Quantitative Saccharomyces cerevisiae Proteome. *Cell Syst* **6**, 192-205.e3 (2018).

4. Fu, J., Warmflash, A. & Lutolf, M. P. Stem-cell-based embryo models for fundamental research and translation. *Nat. Mater.* **20**, 132–144 (2021).

5. Kusserow, A. *et al.* Unexpected complexity of the Wnt gene family in a sea anemone. *Nature* **433**, 156–160 (2005).

6. Serafino, A. *et al.* Developing drugs that target the Wnt pathway: recent approaches in cancer and neurodegenerative diseases. *Expert Opin. Drug Discov.* **12**, 169–186 (2017).

7. Clevers, H. Wnt/β-Catenin Signaling in Development and Disease. *Cell* **127**, 469–480 (2006).

8. Schaefer, K. N. & Peifer, M. Wnt/Beta-Catenin Signaling Regulation and a Role for Biomolecular Condensates. *Dev. Cell* **48**, 429–444 (2019).

9. Pronobis, M. I., Rusan, N. M. & Peifer, M. A novel GSK3-regulated APC:Axin interaction regulates Wnt signaling by driving a catalytic cycle of efficient βcatenin destruction. *Elife* **4**, 1–31 (2015).

10. Boeynaems, S. *et al.* Protein Phase Separation: A New Phase in Cell Biology. *Trends Cell Biol.* **28**, 420–435 (2018).

11. André, A. A. M. & Spruijt, E. Liquid-Liquid Phase Separation in Crowded Environments. *Int. J. Mol. Sci.* **21**, (2020).

12. Youn, J.-Y. *et al.* Properties of Stress Granule and P-Body Proteomes. *Mol. Cell* **76**, 286–294 (2019).

13. Hofmann, S., Kedersha, N., Anderson, P. & Ivanov, P. Molecular mechanisms of stress granule assembly and disassembly. *Biochim. Biophys. Acta Mol. Cell Res.* **1868**, 118876 (2021).

14. Su, Q., Mehta, S. & Zhang, J. Liquid-liquid phase separation: Orchestrating cell signaling through time and space. *Mol. Cell* **81**, 4137–4146 (2021).

15. Ramberger, E. *et al.* PRISMA and BioID disclose a motifs-based interactome of the intrinsically disordered transcription factor C/EBPα. *iScience* **24**, 102686 (2021).

16. Cerami, E. *et al.* The cBio cancer genomics portal: an open platform for exploring multidimensional cancer genomics data. *Cancer Discov.* **2**, 401–404 (2012).

17. Schaefer, K. N. *et al.* Supramolecular assembly of the beta-catenin destruction complex and the effect of Wnt signaling on its localization, molecular size, and activity in vivo. *PLoS Genet.* **14**, 1–44 (2018).

18. Xu, M., Liu, X., Xu, Y., Zhu, S. & Gao, Y. Co-expression of Axin and APC gene fragments inhibits colorectal cancer cell growth via regulation of the Wnt signaling pathway. *Mol. Med. Rep.* **16**, 3783–3790 (2017).

19. Nusse, R. & Clevers, H. Wnt/β-Catenin Signaling, Disease, and Emerging Therapeutic Modalities. *Cell* **169**, 985–999 (2017).

20. Li, V. S. W. *et al.* Wnt Signaling through Inhibition of β-Catenin Degradation in an Intact Axin1 Complex. *Cell* **149**, 1245–1256 (2012).

21. Cliffe, A., Hamada, F. & Bienz, M. A Role of Dishevelled in Relocating Axin to the Plasma Membrane during Wingless Signaling. *Curr. Biol.* **13**, 960–966 (2003).

22. Bugaj, L. J., Choksi, A. T., Mesuda, C. K., Kane, R. S. & Schaffer, D. V. Optogenetic protein clustering and signaling activation in mammalian cells. *Nat. Methods* **10**, 249–252 (2013).

23. Nong, J. *et al.* Phase separation of Axin organizes the β-catenin destruction complex. *J. Cell Biol.* **220**, (2021).

24. Roberts, D. M. *et al.* Defining components of the ßcatenin destruction complex and exploring its regulation and mechanisms of action during development. *PLoS One* **7**, (2012).

25. Kan, W. *et al.* Limited dishevelled/Axin oligomerization determines efficiency of Wnt/β-catenin signal transduction. *Elife* **9**, (2020).

26. Roberts, D. M. *et al.* Deconstructing the βcatenin destruction complex: mechanistic roles for the tumor suppressor APC in regulating Wnt signaling. *Mol. Biol. Cell* **22**, 1845–1863 (2011).

27. Yamanishi, K. *et al.* A direct heterotypic interaction between theDIX domains of Dishevelled and Axin mediates signaling to β-catenin. *Science Signaling* **12**, 1–8 (2019).

28. Bashor, C. J., Helman, N. C., Yan, S. & Lim, W. A. Using engineered scaffold interactions to reshape MAP kinase pathway signaling dynamics. *Science* **319**, 1539–1543 (2008).

29. Shimobayashi, S. F., Ronceray, P., Sanders, D. W., Haataja, M. P. & Brangwynne, C. P. Nucleation landscape of biomolecular condensates. *Nature* 1–4 (2021).

30. Shin, Y. *et al.* Spatiotemporal Control of Intracellular Phase Transitions Using Light-Activated optoDroplets. *Cell* **168**, 159-171.e14 (2017).

31. Weber, S. C. & Brangwynne, C. P. Inverse size scaling of the nucleolus by a concentration-dependent phase transition. *Curr. Biol.* **25**, 641–646 (2015).

32. Lin, Y. *et al.* Narrow equilibrium window for complex coacervation of tau and RNA under cellular conditions. *Elife* **8**, 1–31 (2019).

33. Mora, T. & Bialek, W. Are Biological Systems Poised at Criticality? *J. Stat. Phys.* **144**, 268–302 (2011).

34. Vora, S. M., Fassler, J. S. & Phillips, B. T. Centrosomes are required for proper β-catenin processing and Wnt response. *Mol. Biol. Cell* **31**, 1951–1961 (2020).

35. Kaplan, D. D., Meigs, T. E., Kelly, P. & Casey, P. J. Identification of a role for beta-catenin in the establishment of a bipolar mitotic spindle. *J. Biol. Chem.* **279**, 10829–10832 (2004).

36. Ruan, K. *et al.* PLK1 interacts and phosphorylates Axin that is essential for proper centrosome formation. *PLoS One* **7**, e49184 (2012).

37. Lui, C., Mok, M. T. S. & Henderson, B. R. Characterization of Adenomatous Polyposis Coli Protein Dynamics and Localization at the Centrosome. *Cancers* **8**, (2016).

38. Cunha-Ferreira, I. *et al.* The SCF/Slimb ubiquitin ligase limits centrosome amplification through degradation of SAK/PLK4. *Curr. Biol.* **19**, 43–49 (2009).

39. Munemitsu, S. *et al.* The APC gene product associates with microtubules in vivo and promotes their assembly in vitro. *Cancer Res.* **54**, 3676–3681 (1994).

40. Alberti, S., Gladfelter, A. & Mittag, T. Considerations and Challenges in Studying Liquid-Liquid Phase Separation and Biomolecular Condensates. *Cell* vol. 176 419–434 Preprint at https://doi.org/10.1016/j.cell.2018.12.035 (2019).

41. Schwarz-Romond, T., Metcalfe, C. & Bienz, M. Dynamic recruitment of axin by Dishevelled protein assemblies. *J. Cell Sci.* **120**, 2402–2412 (2007).

42. Elmore, Z. C., Guillen, R. X. & Gould, K. L. The kinase domain of CK1 enzymes contains the localization cue essential for compartmentalized signaling at the spindle pole. *Mol. Biol. Cell* **29**, 1664–1674 (2018).

43. Mbom, B. C., Nelson, W. J. & Barth, A. B-catenin at the centrosome: Discrete pools of β-catenin communicate during mitosis and may co-ordinate centrosome functions and cell cycle progression. *Bioessays* **35**, 804–809 (2013).

44. Fumoto, K., Kadono, M., Izumi, N. & Kikuchi, A. Axin localizes to the centrosome and is involved in microtubule nucleation. *EMBO Rep.* **10**, 606–613 (2009).

45. O'Flynn, B. G. & Mittag, T. A new phase for enzyme kinetics. *Nat. Chem. Biol.* **17**, 628–630 (2021).

46. McSwiggen, D. T., Mir, M., Darzacq, X. & Tjian, R. Evaluating phase separation in live cells: diagnosis, caveats, and functional consequences. *Genes Dev.* **33**, 1619–1634 (2019).

47. Liu, C. *et al.* Control of beta-catenin phosphorylation/degradation by a dual-kinase mechanism. *Cell* **108**, 837–847 (2002).

48. Fiol, C. J., Wang, A., Roeske, R. W. & Roach, P. J. Ordered multisite protein phosphorylation. Analysis of glycogen synthase kinase 3 action using model peptide substrates. *J. Biol. Chem.* **265**, 6061–6065 (1990).

49. Pronobis, M. I., Deuitch, N., Posham, V., Mimori-Kiyosue, Y. & Peifer, M. Reconstituting regulation of the canonical Wnt pathway by engineering a minimal β-catenin destruction machine. *Mol. Biol. Cell* **28**, 41–53 (2016).

50. Rosenbloom, A. B. *et al.* β-Catenin signaling dynamics regulate cell fate in differentiating neural stem cells. *Proc. Natl. Acad. Sci. U. S. A.* (2020) doi:10.1073/pnas.2008509117.

51. Bracha, D. *et al.* Mapping Local and Global Liquid Phase Behavior in Living Cells Using Photo-Oligomerizable Seeds. *Cell* **175**, 1467-1480.e13 (2018).

52. Lindsley, R. C., Gill, J. G., Kyba, M., Murphy, T. L. & Murphy, K. M. Canonical Wnt signaling is required for development of embryonic stem cell-derived mesoderm. *Development* **133**, 3787–3796 (2006).

53. Thomson, M. *et al.* Pluripotency factors in embryonic stem cells regulate differentiation into germ layers. *Cell* **145**, 875–889 (2011).

54. Lee, E., Salic, A., Krü Ger, R., Heinrich, R. & Kirschner, M. W. The Roles of APC and Axin Derived from Experimental and Theoretical Analysis of the Wnt Pathway. doi:10.1371/journal.pbio.0000010.

55. Li, T.-M. *et al.* Multivalent tumor suppressor adenomatous polyposis coli promotes Axin biomolecular condensate formation and efficient β-catenin degradation. *Sci. Rep.* **10**, 17425 (2020).

56. Zeng, X. *et al.* Initiation of Wnt signaling: control of Wnt coreceptor Lrp6 phosphorylation/activation via frizzled, dishevelled and axin functions. *Development* **135**, 367–375 (2008).

57. Niehrs, C. & Shen, J. Regulation of Lrp6 phosphorylation. *Cell. Mol. Life Sci.* **67**, 2551–2562 (2010).

58. Lui, C., Ashton, C., Sharma, M., Brocardo, M. G. & Henderson, B. R. APC functions at the centrosome to stimulate microtubule growth. *Int. J. Biochem. Cell Biol.* **70**, 39–47 (2016).

59. Bazzi, H. & Anderson, K. V. Acentriolar mitosis activates a p53-dependent apoptosis pathway in the mouse embryo. *Proc. Natl. Acad. Sci. U. S. A.* **111**, E1491-500 (2014).

60. Basto, R. *et al.* Flies without centrioles. *Cell* **125**, 1375–1386 (2006).

61. Perbal, B. *A practical guide to molecular cloning*. (John Wiley and Sons Inc., New York, 1988).

62. General Transfection. https://www.addgene.org/protocols/transfection/.

63. Addgene: Zhang Lab CRISPR Page. https://www.addgene.org/crispr/zhang/.

64. Immunocytochemistry and immunofluorescence protocol. https://www.abcam.com/protocols/immunocytochemistry-immunofluorescence-protocol (2021).

65. Western blot protocol. https://www.abcam.com/protocols/general-western-blot-protocol (2021).

66. Bugaj, L. J. & Lim, W. A. High-throughput multicolor optogenetics in microwell plates. *Nat. Protoc.* **14**, 2205–2228 (2019).

67. Berry, J., Brangwynne, C. P. & Haataja, M. Physical principles of intracellular organization via active and passive phase transitions. *Rep. Prog. Phys.* **81**, 046601 (2018).

68. Lutsko, J. F. Mechanism for the stabilization of protein clusters above the solubility curve: the role of non-ideal chemical reactions. *arXiv [physics.chem-ph]* (2016).

69. Berry, J., Weber, S. C., Vaidya, N., Haataja, M. & Brangwynne, C. P. RNA transcription modulates phase transition-driven nuclear body assembly. *Proc. Natl. Acad. Sci. U. S. A.* **112**, E5237–E5245 (2015).

70. https://fenicsproject.org/olddocs/dolfin/1.3.0/python/demo/documented/cahn-hilliard/python/documentation.html#.

71. Naji, A. *et al.* Biological functions of mesenchymal stem cells and clinical implications. *Cell. Mol. Life Sci.* **76**, 3323–3348 (2019).

72. Zhu, G., Hu, J. & Xi, R. The cellular niche for intestinal stem cells: a team effort. *Cell Regen* **10**, 1 (2021).

73. Intlekofer, A. M. & Finley, L. W. S. Metabolic signatures of cancer cells and stem cells. *Nat Metab* **1**, 177–188 (2019).

74. Barati, M. *et al.* Pluripotent Stem Cells: Cancer Study, Therapy, and Vaccination. *Stem Cell Rev Rep* **17**, 1975–1992 (2021).

75. Ruiz, S. *et al.* A high proliferation rate is required for cell reprogramming and maintenance of human embryonic stem cell identity. *Curr. Biol.* **21**, 45–52 (2011).

76. McCarthy, N., Kraiczy, J. & Shivdasani, R. A. Cellular and molecular architecture of the intestinal stem cell niche. *Nat. Cell Biol.* **22**, 1033–1041 (2020).

77. Simsek, M. F. & Özbudak, E. M. Patterning principles of morphogen gradients. *Open Biol.* **12**, 220224 (2022).

78. Liu, J. *et al.* Wnt/β-catenin signalling: function, biological mechanisms, and therapeutic opportunities. *Signal Transduct Target Ther* **7**, 3 (2022).

79. van Amerongen, R. & Nusse, R. Towards an integrated view of Wnt signaling in development. *Development* **136**, 3205–3214 (2009).

80. Repina, N. A. *et al.* Engineered Illumination Devices for Optogenetic Control of Cellular Signaling Dynamics. *Cell Rep.* **31**, 107737 (2020).

81. Heppt, J. *et al.* β-catenin signaling modulates the tempo of dendritic growth of adult-born hippocampal neurons. *EMBO J.* **39**, e104472 (2020).

82. Farin, H. F. *et al.* Visualization of a short-range Wnt gradient in the intestinal stem-cell niche. *Nature* **530**, 340–343 (2016).

83. Hopfield, J. J. Kinetic proofreading: a new mechanism for reducing errors in biosynthetic processes requiring high specificity. *Proc. Natl. Acad. Sci. U. S. A.* **71**, 4135–4139 (1974).

84. Bryja, V., Červenka, I. & Čajánek, L. The connections of Wnt pathway components with cell cycle and centrosome: side effects or a hidden logic? *Crit. Rev. Biochem. Mol. Biol.* **52**, 614–637 (2017).

85. Lach, R. S. *et al.* Nucleation of the destruction complex on the centrosome accelerates degradation of β-catenin and regulates Wnt signal transmission. *Proc. Natl. Acad. Sci. U. S. A.* **119**, e2204688119 (2022).

86. Schubert, A. *et al.* Superresolution microscopy localizes endogenous Dvl2 to Wnt signaling-responsive biomolecular condensates. *Proc. Natl. Acad. Sci. U. S. A.* **119**, e2122476119 (2022).

87. Davidson, G. *et al.* Cell cycle control of wnt receptor activation. *Dev. Cell* **17**, 788–799 (2009).

88. Sakaue-Sawano, A. *et al.* Visualizing spatiotemporal dynamics of multicellular cell-cycle progression. *Cell* **132**, 487–498 (2008).

89. Pagella, P. *et al.* The time-resolved genomic impact of Wnt/β-catenin signaling. *Cell Syst* **14**, 563-581.e7 (2023).

90. Höhener, T. C. *et al.* LITOS: a versatile LED illumination tool for optogenetic stimulation. *Sci. Rep.* **12**, 13139 (2022).

91. Hamis, S. J. *et al.* Quantifying ERK activity in response to inhibition of the BRAFV600E-MEK-ERK cascade using mathematical modelling. *Br. J. Cancer* **125**, 1552–1560 (2021).

92. Gammons, M. & Bienz, M. Multiprotein complexes governing Wnt signal transduction. *Curr. Opin. Cell Biol.* **51**, 42–49 (2018).

93. Lee, G., White, L. S., Hurov, K. E., Stappenbeck, T. S. & Piwnica-Worms, H. Response of small intestinal epithelial cells to acute disruption of cell division through CDC25 deletion. *Proc. Natl. Acad. Sci. U. S. A.* **106**, 4701–4706 (2009).

94. Stringer, C., Wang, T., Michaelos, M. & Pachitariu, M. Cellpose: a generalist algorithm for cellular segmentation. *Nat. Methods* **18**, 100–106 (2021).

95. Ershov, D. *et al.* TrackMate 7: integrating state-of-the-art segmentation algorithms into tracking pipelines. *Nat. Methods* **19**, 829–832 (2022).